Computer Modeling in Engineering & Sciences

Tech Science Press

DOI: 10.32604/cmes.2024.055963

ARTICLE

An SPH Framework for Earthquake-Induced Liquefaction Hazard Assessment of Geotechnical Structures

Sourabh Mhaski* **and G. V. Ramana**

Department of Civil Engineering, Indian Institute of Technology Delhi, New Delhi, 110016, India

*Corresponding Author: Sourabh Mhaski. Email: sourabhmhaski@civil.iitd.ac.in

Received: 11 July 2024 Accepted: 23 October 2024 Published: 17 December 2024

ABSTRACT

Earthquake-induced soil liquefaction poses significant risks to the stability of geotechnical structures worldwide. An understanding of the liquefaction triggering, and the post-failure large deformation behaviour is essential for designing resilient infrastructure. The present study develops a Smoothed Particle Hydrodynamics (SPH) framework for earthquake-induced liquefaction hazard assessment of geotechnical structures. The coupled flow-deformation behaviour of soils subjected to cyclic loading is described using the PM4Sand model implemented in a three-phase, single-layer SPH framework. A staggered discretisation scheme based on the stress particle SPH approach is adopted to minimise numerical inaccuracies caused by zero-energy modes and tensile instability. Further, non-reflecting boundary conditions for seismic analysis of semi-infinite soil domains using the SPH method are proposed. The numerical framework is employed for the analysis of cyclic direct simple shear test, seismic analysis of a level ground site, and liquefaction-induced failure of the Lower San Fernando Dam. Satisfactory agreement for liquefaction triggering and post-failure behaviour demonstrates that the SPH framework can be utilised to assess the effect of seismic loading on field-scale geotechnical structures. The present study also serves as the basis for future advancements of the SPH method for applications related to earthquake geotechnical engineering.

KEYWORDS

Earthquake; seismic; liquefaction; stress particle; PM4Sand; smoothed particle hydrodynamics (SPH)

1 Introduction

Soil liquefaction is characterised by the development of excess pore-water pressure under undrained conditions and the associated loss of shear strength [1]. Liquefaction is often triggered by earthquakes and may compromise the stability of geotechnical structures such as earth dams, retaining walls, ash ponds, mine tailings dams, etc. In addition to the infrastructural damage, these failures can also transform into large deformation mass flow events due to the saturated and weakened state of the material, further amplifying the liquefaction hazard. Over the years, several documented earthquake events [2–9] have highlighted the need for designing geotechnical structures resilient to such failures. This requires an understanding of both the triggering of liquefaction and the post-liquefaction large deformation behaviour.

Traditionally, the liquefaction potential of a soil deposit has been assessed using the cyclic stress ratio approach (also known as the simplified approach) based on comparing the earthquake-induced cyclic shear stresses with the liquefaction resistance of the soil [10]. The shear stresses induced by the earthquake are commonly evaluated using an equivalent linear analysis of the soil deposit [1]. Although frequently adopted in engineering practice, the approach presents limitations such as providing no information regarding the development of excess pore-water pressure, relying on indirect estimates of earthquake-induced deformations using empirical correlations, and utilising linear analysis to approximate the nonlinear and irreversible soil behaviour. Generally, nonlinear analyses employing elastoplastic soil constitutive models in an effective stress framework are considered the state-of-the-art approach for assessing liquefaction hazards [11–13]. Mesh-based techniques (e.g., Finite Element Method (FEM) or Finite Difference Method (FDM)) are routinely adopted for the nonlinear seismic analysis of geotechnical structures, e.g., FEM [14–18] and FDM [19,20]. Despite their utility, these methods cater to small deformation regimes and are susceptible to mesh distortion during the post-failure large deformation analysis unless advanced approaches such as Coupled Eulerian-Lagrangian (CEL) or Arbitrary Lagrangian-Eulerian (ALE) are adopted [21–23].

Alternatively, meshless numerical techniques (e.g., Discrete Element Method (DEM), Material Point Method (MPM), and Smoothed Particle Hydrodynamics (SPH)) are being increasingly utilised for modeling large deformation scenarios in geotechnical engineering [24–27]. With regards to liquefaction modelling, the DEM combined with a fluid solver offers valuable micromechanical insights into soil liquefaction [28–30]. However, the application of DEM to practical, field-scale problems is often limited due to high computational costs, and continuum-scale approaches (MPM and SPH) are more suited for such scenarios. The MPM has been extensively adopted to investigate the effects of seismic loading on geotechnical structures and natural formations [31–35].

In comparison, the applicability of the SPH method for earthquake geotechnical engineering has been less well explored. The SPH method has been primarily adopted for analysing seismically induced slope instabilities [36–40] and the subsequent large deformation mass flow behaviour [41,42]. Barring a few exceptions (e.g., [39,40]), the previous studies were based on the single-phase SPH framework and employed elastoplastic soil constitutive models developed for static analysis to describe the soil behaviour under cyclic loading conditions. Although sufficiently accurate for inertial slope instability and rapid (undrained) mass flows, such an approach is inadequate for modelling soil liquefaction, wherein a coupled soil-fluid framework with appropriate soil constitutive models is essential for capturing the pore-water pressure accumulation and progressive degradation of soil stiffness and shear strength [13]. Another critical issue is the modelling of boundary conditions during seismic analysis. In the previously mentioned studies, the earthquake acceleration or velocity history was directly imposed on the model extremities, resulting in rigid and reflective boundaries. In reality, soil domains are unbounded (semi-infinite) unless bedrock is present at a shallow depth. Consequently, the outward propagating stress waves are not reflected and will be dissipated by material and radiation damping. Such a condition may be approximated by placing the numerical boundaries sufficiently far away from the region of interest, however, at the expense of the computational efficiency of the analysis. Alternatively, boundary conditions with non-reflecting (absorbing) characteristics are employed for the seismic analysis of geotechnical structures in semi-infinite domains [13]. However, non-reflecting boundary conditions for seismic analysis in the framework of SPH have not yet been formulated.

The present study develops an SPH framework for the earthquake-induced liquefaction hazard assessment of geotechnical structures. The critical state-based soil constitutive model PM4Sand [43,44] is implemented in a three-phase, single-layer SPH framework [45] to model the behaviour of saturated or unsaturated soils subjected to cyclic loading. The mathematical model is solved using the stress

particle SPH approach [46,47] to minimise the effects of the zero-energy modes and tensile instability on the numerical solution. Additionally, non-reflecting boundary conditions appropriate for seismic analysis using the SPH method are proposed. The implementation of the PM4Sand model in the SPH framework is verified by simulating cyclic direct simple shear test. Subsequently, the non-reflecting boundary conditions are validated by seismic analysis of a level ground. Finally, the capability of the SPH framework for the analysis of a complex geotechnical structure is demonstrated by analysing the liquefaction-induced failure of the Lower San Fernando Dam.

2 Mathematical Model

2.1 Governing Equations

In the present study, the soil mixture consists of three phases, solid skeleton (s), water (f), and air (a), and is described using the $u-p$ formulation of governing equations [13]. Further, the solid grains are incompressible, water is weakly compressible and elastic, while the air phase is inactive (i.e., air pressure, $p_a \approx 0$). The final form of the governing equations is listed below, while the detailed derivations can be found in [13,45].

$$\frac{d^s n}{dt} = (1-n)\,\nabla \cdot \boldsymbol{v} \tag{1}$$

$$\frac{d^s \boldsymbol{v}}{dt} = \frac{1}{\rho_m}\nabla \cdot \sigma + \boldsymbol{b} \tag{2}$$

$$\frac{d^s h_p}{dt} = \frac{1}{\tilde{C}_{sr}}\left(\nabla \cdot (\boldsymbol{k}\nabla H) + \nabla \cdot \left(\frac{\boldsymbol{k}}{g}\frac{d^s \boldsymbol{v}}{dt}\right) - S_r \nabla \cdot \boldsymbol{v}\right) \tag{3}$$

$$\frac{d^s \epsilon}{dt} = \frac{1}{2}\left(\boldsymbol{v} \otimes \nabla + \nabla \otimes \boldsymbol{v}\right); \frac{d^s \omega}{dt} = \frac{1}{2}\left(\boldsymbol{v} \otimes \nabla - \nabla \otimes \boldsymbol{v}\right) \tag{4}$$

In the above equations, n is the porosity, $\boldsymbol{v}$ is the velocity of the solid skeleton, ρ_m is the density of the mixture, $\sigma = \sigma' - S_r p_f \boldsymbol{I}$ is the Cauchy stress tensor, with σ', S_r, p_f, and $\boldsymbol{b}$ being the effective stress tensor, degree of saturation, pore-fluid pressure, and body force vector, respectively. For the flow model (Eq. (3)), $h_p = p_f/\gamma_f$ is the pressure head, γ_f is the unit weight of water, $\tilde{C}_{sr} = C_l + C_s$ with $C_l = nS_r\gamma_f/K_f$ and $C_s = n(d^s S_r/dh_p)$. K_f is the bulk modulus of water, $\boldsymbol{k}$ is the hydraulic conductivity tensor and $H = h_p + y$ is the total head. The degree of saturation is related to the pressure head (h_p) using the van Genuchten model [48]. Further, ϵ and ω are the strain and spin tensors, respectively, while the superscript s denotes that the governing equations are derived on the reference frame of the solid skeleton. In addition to the governing equations listed above, an accurate description of the constitutive behaviour of the soil subjected to cyclic loading is essential for capturing liquefaction.

2.2 Soil Constitutive Model

The PM4Sand model [43,44] is used to describe the behaviour of liquefiable soils subjected to cyclic loading. PM4Sand is a two-dimensional (plane strain) soil model developed based on the bounding surface plasticity approach [49,50]. The model comprises four surfaces in the effective stress space: (i) yield surface, (ii) critical state surface, (iii) bounding surface, and (iv) dilatancy surface. The bounding surface governs the peak angle of the shearing resistance of the soil, whereas the dilatancy surface delineates the contractive and dilative behaviours. The nonlinear soil response under cyclic loading is simulated by updating the bounding and dilatancy surfaces based on a relative state parameter index. The two surfaces converge to the critical state surface as the soil attains a critical state.

The calibration of the PM4Sand model requires three primary parameters: (i) relative density of the soil, D_r, (ii) small strain shear modulus coefficient, G_0, and (iii) contraction rate parameter, h_{p0}, along with sixteen secondary parameters. The parameters D_r and G_0 can be estimated using field or experimental investigations. Subsequently, the parameter h_{p0} is iteratively calibrated to match the target cyclic resistance ratio (CRR) for the soil based on liquefaction-triggering correlations. Detailed formulations, numerical implementation, and calibration of the PM4Sand model are discussed in several References [44,51,52] and are not repeated here. In the present study, stress update for the PM4Sand model is performed using the fourth-order Runge-Kutta method [51]. Moreover, as the objective of the present study is to develop an SPH framework for liquefaction hazard assessment of geotechnical structures, the primary calibration parameters for PM4Sand available in the literature are adopted for the numerical examples discussed in Section 6. Further, default values of the secondary calibration parameters are utilised following the recommendation of Ziotopoulou et al. [44]. The non-liquefiable soils are described using the non-associative Drucker Prager model. The stress update procedure for the same using the second-order leapfrog method can be found in [26]. Additionally, the Jaumann stress rate [45,53] is adopted to maintain the objectivity of constitutive equations.

3 Spatial Discretisation of Governing Equations

The SPH method is adopted for the numerical solution of the mathematical model described in Section 2. The fundamental aspects of the SPH method have been discussed in several studies [26,54,55]. The present section focuses on the spatial discretisation of the governing equations using the stress particle SPH approach [46,47].

Two sets of particles or nodes called the velocity nodes (vn) and stress nodes (sn), are utilised for the solution of the mathematical model (Section 2). A typical arrangement of velocity and stress nodes is shown in Fig. 1, where two stress nodes are placed diagonally with respect to a velocity node. The velocity ($\boldsymbol{v}$) and pressure (p_f) fields are solved on the velocity nodes, whereas the constitutive equations (for effective stress σ') are solved on the stress nodes. As the velocity field is solved on the velocity nodes, the position of velocity nodes is updated using explicit time integration and represents the material deformation. On the other hand, the stress nodes follow the linked velocity node throughout the simulation, maintaining the same relative configuration (Fig. 1). Chalk et al. [46] demonstrated that the staggered solution for the velocity and stress fields using the stress particle approach minimises the numerical inaccuracies associated with zero-energy modes and tensile instability in an SPH analysis. The discretised form of the governing equations is as follows [45]:

$$\left(\frac{d^s n}{dt}\right)_{i\in vn} = \sum_{j\in vn} \frac{m_j}{\rho_j}\left(1-n_j\right)\boldsymbol{v}_{ji}\cdot\tilde{\nabla}_i W_{ij} \tag{5}$$

$$\left(\frac{d^s \boldsymbol{v}}{dt}\right)_{i\in vn} = \left(\frac{\rho_i}{\rho_{mi}}\right)\sum_{j\in sn} m_j\left(\frac{\sigma_i^{'}}{\rho_i^2}+\frac{\sigma_j^{'}}{\rho_j^2}\right)\cdot\nabla_i W_{ij} - \left(\frac{\rho_i}{\rho_{mi}}\right)\sum_{j\in vn} m_j\left(\frac{S_{ri}p_{fi}}{\rho_i^2}+\frac{S_{rj}p_{fj}}{\rho_j^2}\right)\nabla_i W_{ij} + \boldsymbol{b}_i \tag{6}$$

$$\begin{aligned}\left(\frac{d^s h_p}{dt}\right)_{i\in vn} = {} & \frac{1}{\tilde{C}_{sri}}\left(\sum_{j\in vn}\frac{m_j}{\rho_j}\overline{k}_{ij}^{mn}H_{ji}D^{mn}\tilde{F}_{ij} - k_i^{mn}\tilde{\nabla}H_i\cdot\sum_{j\in vn}\frac{m_j}{\rho_j}\boldsymbol{x}_{ji}D^{mn}\tilde{F}_{ij}\right)\\ & + \frac{1}{\tilde{C}_{sri}}\left(\frac{1}{g}\sum_{j\in vn}\frac{m_j}{\rho_j}\overline{k}_{ij}^{mn}\frac{d\boldsymbol{v}_{ji}^n}{dt}\tilde{\nabla}_i W_{ij} - S_{ri}\sum_{j\in vn}\frac{m_j}{\rho_j}\boldsymbol{v}_{ji}\cdot\tilde{\nabla}_i W_{ij}\right)\end{aligned} \tag{7}$$

$$\left(\frac{d^s\epsilon}{dt}, \frac{d^s\omega}{dt}\right)_{i\in sn} = \frac{1}{2}\sum_{j\in vn}\frac{m_j}{\rho_j}\left(\boldsymbol{v}_{ji}^m\tilde{\nabla}_i W_{ij}^n \pm \boldsymbol{v}_{ji}^n\tilde{\nabla}_i W_{ij}^m\right) \tag{8}$$

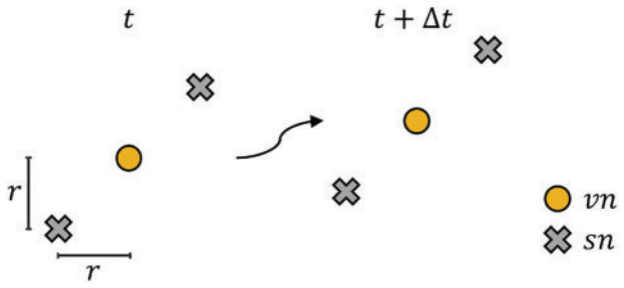

Figure 1: Stress particle SPH discretisation (modified after [46])

In the above equations, (i, j) denote the SPH particle indices, (m, n) are the coordinate directions, m_j and ρ_j are the mass and density of solid skeleton for particle j, $\bar{\boldsymbol{k}}_{ij} = (\boldsymbol{k}_i + \boldsymbol{k}_j)/2$ is the average hydraulic conductivity tensor, $H_{ji} = H_j - H_i$, $\boldsymbol{x}_{ji} = \boldsymbol{x}_j - \boldsymbol{x}_i$, $\boldsymbol{v}_{ji} = \boldsymbol{v}_j - \boldsymbol{v}_i$, and g is the magnitude of the acceleration due to gravity. $W_{ij} = W(\boldsymbol{x}_i - \boldsymbol{x}_j, h)$ is the quintic Wendland kernel function [56], with h being the smoothing length. Throughout this study, $h = 1.4\,\Delta x$, where Δx is the initial particle spacing. Further, $\tilde{\nabla}_i W_{ij} = \boldsymbol{L}_{ij}\nabla_i W_{ij}$ is the corrected kernel gradient, where $\boldsymbol{L}_{ij} = \left[\sum_j (m_j/\rho_j)\boldsymbol{x}_{ji}^m \nabla_i^n W_{ij}\right]^{-1}$ is the gradient correction matrix, $\nabla_i W_{ij}$ is the kernel gradient, $D^{mn} = 4\boldsymbol{x}_{ji}^m \boldsymbol{x}_{ji}^n / |\boldsymbol{x}_{ji}|^2 - \delta^{mn}$, and $\tilde{F}_{ij} = \boldsymbol{x}_{ji}\cdot\tilde{\nabla}_i W_{ij}/|\boldsymbol{x}_{ji}|^2$. Other symbols carry the same meaning as defined in Section 2. Lastly, the artificial viscosity stabilisation term is included in Eq. (6) to suppress any spurious particle oscillations [53].

The approximation for the acceleration due to pressure gradient (i.e., the second term on the right-hand side of Eq. (6)) ensures symmetry of interaction between a particle pair. However, Eq. (6) may result in an incorrect uplift force on particles near the soil free surface. The numerical instability is particularly significant for scenarios where ponded water is present over the soil free surface (e.g., along the upstream face of an earth dam). The uplift occurs as Eq. (6) fails to incorporate the weight of water overlying the soil free surface due to kernel truncation issue [57]. Bui et al. [57] modified the pressure gradient approximation to achieve a vanishing gradient of a constant pressure field. However, such an approximation does not yield a symmetric particle interaction. In the present study, the first-order consistent gradient approximation [58,59] is adopted wherein the gradient of the field variable $f = S_r p_f$ at particle i is obtained by solving the following set of linear equations:

$$\left(\sum_j \frac{m_j}{\rho_j}\begin{bmatrix} W_{ij} & x_{ji}W_{ij} & y_{ji}W_{ij} \\ \nabla_i W_{ij}^x & x_{ji}\nabla_i W_{ij}^x & y_{ji}\nabla_i W_{ij}^x \\ \nabla_i W_{ij}^y & x_{ji}\nabla_i W_{ij}^y & y_{ji}\nabla_i W_{ij}^y \end{bmatrix}\right)\begin{pmatrix} f_i \\ \partial_x f_i \\ \partial_x f_i \end{pmatrix} = \sum_j \frac{m_j}{\rho_j}\begin{pmatrix} f_j W_{ij} \\ f_j \nabla_i W_{ij}^x \\ f_j \nabla_i W_{ij}^y \end{pmatrix} \tag{9}$$

where the summation is performed over the velocity nodes, $\boldsymbol{x}_{ji} = (x_{ji}, y_{ji})$, and $\partial_m f_i = \partial f_i/\partial x^m$ is the gradient in the coordinate direction m. Additionally, the pressure of the overlying water is imposed on the free-surface submerged particles based on the confining stress boundary condition described in Feng et al. [58]. Lastly, stress particle SPH requires the transfer of information between the stress and velocity nodes (e.g., σ' at the velocity node is required in Eq. (6) and $\boldsymbol{v}$ at the stress node is required in Eq. (8)). The interpolation of a field variable f at node i is performed using the following expression [46]:

$$f_i = \frac{\sum_j \left(m_j/\rho_j\right) f_j W_{ij}}{\sum_j \left(m_j/\rho_j\right) W_{ij}} \tag{10}$$

where if $i \in vn$ then $j \in sn$, and vice-versa. Chalk et al. [46] examined the influence of (i) the number of stress nodes and (ii) the configuration of stress nodes relative to the velocity nodes on the numerical results. They concluded that two stress nodes per velocity node, arranged diagonally in the general direction of the material deformation, provided an optimal balance between numerical accuracy and computational efficiency. Accordingly, the stress node configuration shown in Fig. 1 is adopted throughout this study with $r = \Delta x/3$ where Δx is the initial particle spacing.

4 Boundary Conditions

4.1 Static Analysis

The numerical model for a typical soil slope is shown in Fig. 2a. For the analysis under static loading conditions, the boundary regions are modeled using several layers of fixed boundary particles to avoid kernel truncation for the domain particles (Fig. 2b). Virtual nodes (l) are generated for each boundary particle (b) following the mirroring procedure of Marrone et al. [60]. Subsequently, the essential field variables (i.e., σ' and p_f) are interpolated at the virtual nodes (l) and assigned to the boundary particles (b) as follows [58,61]:

$$\sigma_b'^{mn} = \sigma_l'^{mn} + (x_b - x_l)\,\partial_x \sigma_l'^{mn} + (y_b - y_l)\,\partial_y \sigma_l'^{mn} \tag{11}$$

$$p_{fb} = p_{fl} + (x_b - x_l)\,\partial_x p_{fl} + (y_b - y_l)\,\partial_y p_{fl} \tag{12}$$

where f, $\partial_x f$, and $\partial_y f$ (for $f = \sigma_l'^{mn}$ and p_{fl}), are calculated by solving Eq. (9) at the virtual nodes (l) for interaction with domain velocity nodes (Fig. 2b). Further, a virtual velocity is assigned to the boundary particles to impose the no-slip or free-slip conditions. Specifically, $\boldsymbol{v}_b = -\boldsymbol{v}_l$ for no-slip while $\boldsymbol{v}_b = \boldsymbol{v}_l - (2\boldsymbol{v}_l \cdot \boldsymbol{n})\,\boldsymbol{n}$ for free-slip, where $\boldsymbol{n}$ is the unit vector normal to the boundary, and $\boldsymbol{v}_l$ is the interpolated velocity at the virtual node given by,

$$\boldsymbol{v}_l = \frac{\sum_{j \in vn} \left(m_j/\rho_j\right) \boldsymbol{v}_j W_{lj}}{\sum_{j \in vn} \left(m_j/\rho_j\right) W_{lj}} \tag{13}$$

Hydraulic boundary conditions specifying the pressure (p_f) or pressure head (h_p) in Eq. (7) are imposed on the particles present at the required location. This may necessitate the identification of free-surface particles. In this study, free-surface particles are identified based on the estimated value of divergence of position following the procedure outlined in Mhaski et al. [56].

4.2 Seismic Analysis

As described in the Introduction, boundaries with non-reflecting (absorbing) characteristics are essential for the seismic analysis of semi-infinite domains. Chan et al. [13] described a compliant base boundary condition, wherein the earthquake ground motion is applied to the soil domain as traction time history imposed by the upward propagating stress waves. Further, the downward propagating stress waves are absorbed by viscous dashpots attached to the boundaries in the normal and shear directions [62] (Fig. 2c). The dashpot coefficients are selected to achieve an impedance ratio of one, such that no wave reflection occurs at the boundary [1,13]. In the present study, the compliant base boundary condition is adapted for SPH analysis by applyinsg the acceleration due to ground motion and viscous dashpots to the outermost layer of domain velocity nodes (Fig. 2c) as follows:

$$\left(\frac{d\boldsymbol{v}}{dt}\right)_{i\in vn} = \frac{1}{\rho_m \Delta x}\begin{pmatrix} 2\rho_m C_s v_{su} - \eta_s v_{xi} \\ 2\rho_m C_p v_{pu} - \eta_p v_{yi} \end{pmatrix} \tag{14}$$

where ρ_m is the mixture density, Δx is the particle spacing, (v_{su}, v_{pu}) are the particle speed of upward propagating shear and pressure seismic waves, (v_{xi}, v_{yi}) are the components of the velocity of SPH particle i, $\eta_s = \rho_m C_s$ and $\eta_p = \rho_m C_p$ are the dashpot coefficients, with $C_s = \sqrt{G/\rho_m}$ and $C_p = \sqrt{(K + 4G/3)/\rho_m}$ being the speeds of shear and pressure waves in the soil. The particle velocity of the seismic waves (i.e., v_{su} and v_{pu}) is equal to half of the outcrop motion velocity at the location of the boundary [33]. Further, Factor 2 in Eq. (14) appears as half of the input energy is dissipated by the viscous dashpots. Lastly, to maintain the static equilibrium of the numerical model during the seismic analysis, the effective stress, pressure, and virtual velocity at the boundary particles are interpolated following the procedure described in Section 4.1.

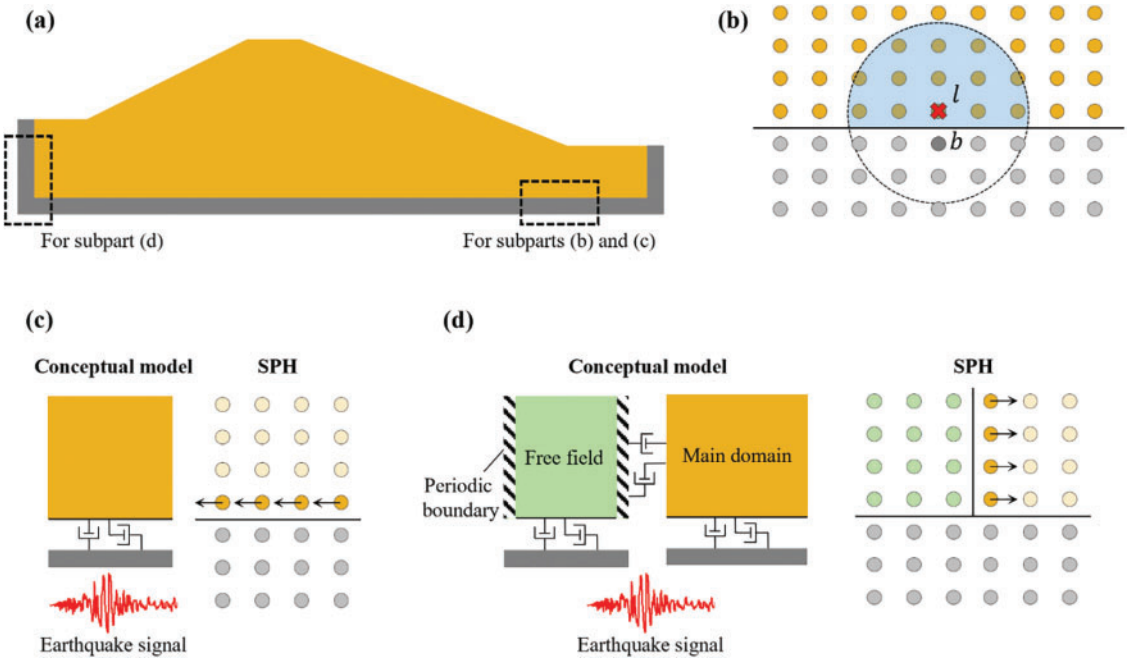

Figure 2: Boundary conditions (a) typical soil slope, (b) static analysis, (c) compliant base boundary, (d) free field boundary for seismic analysis

On the other hand, soil regions beyond the lateral boundaries exhibit free field motion under the action of seismic loading as these regions are far away from any geotechnical structure. Thus, in addition to the non-reflecting (absorbing) characteristics, the lateral boundaries (i) apply tractions on the main domain due to their motion relative to the main domain and (ii) allow the main domain to sway laterally under the effect of the earthquake. In the SPH framework, the fixed lateral boundary particles used during the static analysis are replaced by free field columns (Fig. 2d). The seismic response of the free field columns is analysed independently of the main domain by using periodic boundaries in the lateral direction with ground motion applied by the compliant base boundary condition. In mesh-based methods, the tractions due to the free field motion are applied directly on the nodes of the main domain present near the lateral boundaries [12,13,33]. However, such an approach in SPH was observed to result in stress oscillation near the lateral boundaries due to kernel truncation of the main domain particles. As a result, the approach proposed in the present study is to allow the

main domain particles to interact with the free field particles inside their kernel support radius, but not vice-versa, i.e., the free field motion is not influenced by the main domain. Additionally, to model the absorbing boundary conditions, viscous dashpots are applied to the outermost layer of main domain velocity nodes (Fig. 2d) using the relative velocity of the main domain and free field,

$$\left(\frac{d\boldsymbol{v}}{dt}\right)_{i\in vn} = \frac{1}{\rho_m \Delta x}\begin{pmatrix}\eta_p\left(v_{fxi} - v_{xi}\right)\\ \eta_s\left(v_{fyi} - v_{yi}\right)\end{pmatrix} \tag{15}$$

where $\boldsymbol{v}_{fi} = (v_{fxi}, v_{fyi})$ is the velocity of the free field region at particle i, interpolated using Eq. (10), while other symbols carry the same meaning as defined for Eq. (14).

The numerical implementation of the standard periodic boundary condition and modification required for accurately imposing free field conditions is detailed below. Periodic boundary conditions are modelled by allowing the interaction between particles present on opposite ends of the simulation domain. Further, a particle that leaves the simulation domain from one end is inserted from the opposite end [63]. Although such a boundary is sufficient for modelling the infinite extent of a soil domain, it fails to capture the lateral sway of the soil column under seismic loading. Consequently, the free field particles may overlap with the main domain particles, resulting in inaccurate computations or numerical instability. As a result, in addition to their true coordinates, virtual coordinates are also maintained for the free field particles during the simulation. The virtual coordinates are obtained by advancing the free field particle positions without imposing the periodicity condition, allowing the lateral sway to be modelled. Subsequently, the virtual coordinates are utilised during interaction with the main domain, whereas the free field motion is solved using the true coordinates. The modification to periodic boundary conditions for interaction between the free field and main domain allows accurate and stable imposition of free field conditions, as illustrated in Section 6.

5 Simulation

The numerical framework described in Sections 3 and 4 is implemented in an in-house SPH code developed using the Julia programming language [56,64,65]. Further, local, non-viscous damping [66] is added to the momentum conservation equation (Eq. (6)) during the application of cyclic loading to suppress spurious particle oscillations. The acceleration due to local damping ($\dot{\boldsymbol{v}}_d$) is given by,

$$(\dot{\boldsymbol{v}}_d)_{i\in vn} = -\xi_l \left|\dot{\boldsymbol{v}}_i\right| \operatorname{sign}(\boldsymbol{v}_i) \tag{16}$$

where ξ_l is a coefficient that controls the strength of the damping. The bulk modulus of water (K_l) governs the development of excess pore-water pressure in the soil (Eq. (7)). Unless mentioned otherwise, $K_l = 1.0 \times 10^6$ kPa is adopted for the numerical analyses in Section 6. The earthquake records utilised in this study were obtained from the Pacific Earthquake Engineering Research Center (PEER) ground motion database NGA-West2 [67]. Generally, the time interval of the ground motion record is larger than the timestep used for explicit temporal integration in an SPH analysis. Accordingly, the intermediate acceleration or velocity of the ground motion is calculated by linear interpolation. Field variables (other than the constitutive variables) are updated using the second-order leapfrog algorithm with the maximum timestep for the stability of explicit integration governed by the mechanical and hydraulic criteria, as described in Lian et al. [45].

6 Verification and Validation

6.1 Cyclic Direct Simple Shear Test

The implementation of constitutive models in numerical frameworks designed for liquefaction hazard assessment is generally verified by the simulation of laboratory tests involving predefined stress

paths and boundary conditions [51]. This ensures that the numerical framework can accurately capture the material response under controlled cyclic loading before being utilized for the analysis of more complex initial boundary value problems involving earthquake ground motion. As PM4Sand is a two-dimensional (plane-strain) model, the implementation of the PM4Sand model is verified by simulating the constant volume (undrained) cyclic direct simple shear (DSS) test. For this purpose, the results obtained from the SPH framework are compared to the benchmark results from the well-established finite element package OpenSees [68].

The numerical models are shown in Fig. 3. The SPH model (Fig. 3a) consists of a central region Ω (0.1 m $\times$ 0.1 m), surrounded by a boundary region Γ (0.3 m $\times$ 0.3 m). Spatial discretisation is performed using 900 particles (i.e., 900 velocity nodes and 1800 stress nodes) at an initial spacing $\Delta x = 0.01$ m. In contrast, a single four-node quadrilateral element (SSPquadUP) of size 0.3 m $\times$ 0.3 m is used for the FEM analysis (Fig. 3b). The boundary conditions for the FEM model include full fixity at the base nodes and an equal degree of freedom condition for the top nodes [51].

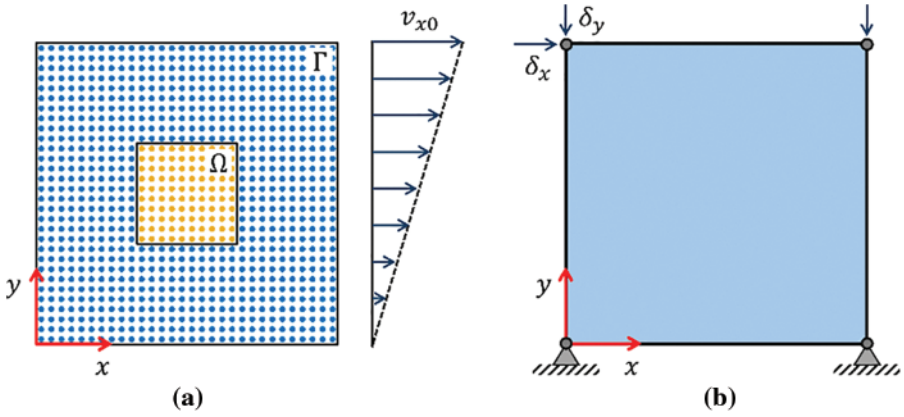

Figure 3: Cyclic direct simple shear configuration during shearing phase (a) SPH, and (b) FEM

The numerical analysis is performed for three initial states of the soil specified by the corrected SPT value $(N_1)_{60}$. The primary calibration parameters for PM4Sand reported in [69] are utilised for the analysis (Table 1). Further, the specific gravity of soil solids $G_s = 2.65$, unit weight of water $\gamma_f = 10$ kNm^{-3} and initial porosity n is calculated based on the relative density D_r. Initial stress state with vertical effective stress $\sigma'_{v0} = 101.3$ kPa and $K_0 = 0.5$ is assigned to the SPH particles. During the shearing phase, the particles in the central region are allowed to move freely, whereas the velocity of the particles in the boundary region is enforced for attaining simple shear conditions in the central region as follows:

$$v_{xi} = v_{x0}\,(y_i/H)\,;\, v_{yi} = 0 \tag{17}$$

where $H = 0.3$ m, and v_{x0} is the velocity of the top plate. The cyclic resistance ratio (CRR) governs the amplitude of cyclic shear stress during the shearing phase and is estimated using SPT-based liquefaction triggering correlation [43]. The average of the shear stress of particles present in the central region (Ω) is used for calculating the cyclic stress ratio (τ_{xy}/σ'_{v0}). If the average cyclic stress ratio exceeds the cyclic resistance ratio, the direction of the top plate velocity (v_{x0}) is reversed following the procedure described in Boulanger et al. [69]. Local damping coefficient $\xi_l = 0.05$ is used for the analysis (Eq. (16)). Further, the velocity of the particles in the central region (Ω) is reinitialised to the analytical value (Eq. (17)) every 2000 computational steps to minimise the influence of spurious particle motion under

cyclic loading conditions. On the other hand, the gravity loading approach is used for achieving the initial stress state in the FEM analysis. During the shearing phase, the confining stress is maintained by equivalent vertical nodal displacement (δ_y), whereas horizontal nodal displacement (δ_x) is applied to impose cyclic simple shear (Fig. 3b). Further details on the FEM analysis can be found in [51].

Table 1: PM4Sand parameters for direct simple shear and seismic analysis of level ground site

$(N_1)_{60}$	CRR	D_r	G_0	h_{p0}
6	0.090	0.35	476	0.53
14	0.147	0.55	677	0.40
26	0.312	0.75	890	0.63

The numerical analysis results are illustrated in Figs. 4 to 6 in terms of the effective stress paths and stress-strain behaviour. The vertical effective stress decreases with the application of cyclic shear stress, ultimately resulting in soil liquefaction (i.e., $\sigma_v^{'} \approx 0$). Further, the soil stiffness is progressively reduced, as observed by the higher shear strain amplitude with increasing loading cycles. Although some discrepancies between the SPH and FEM results are observed, the soil behaviour (e.g., strength degradation and number of loading cycles to liquefaction) is captured with satisfactory accuracy in all cases. The results verify the implementation of the PM4Sand model in the SPH framework, enabling its application towards general initial-boundary value problems.

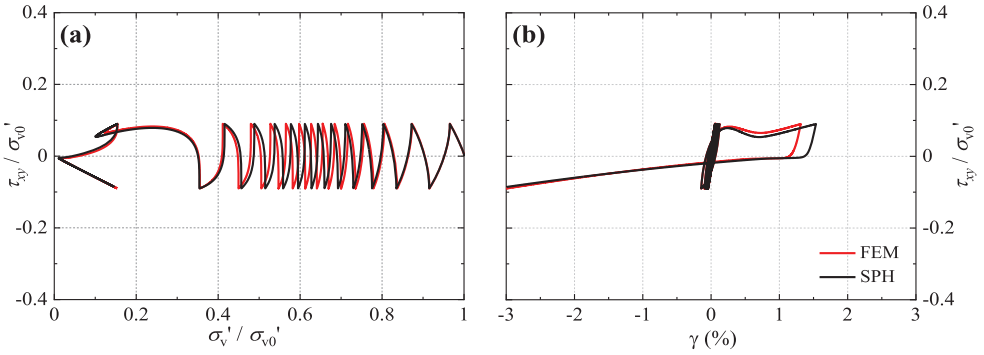

Figure 4: Cyclic direct simple shear at $(N_1)_{60} = 6$ (a) effective stress path and (b) stress-strain response

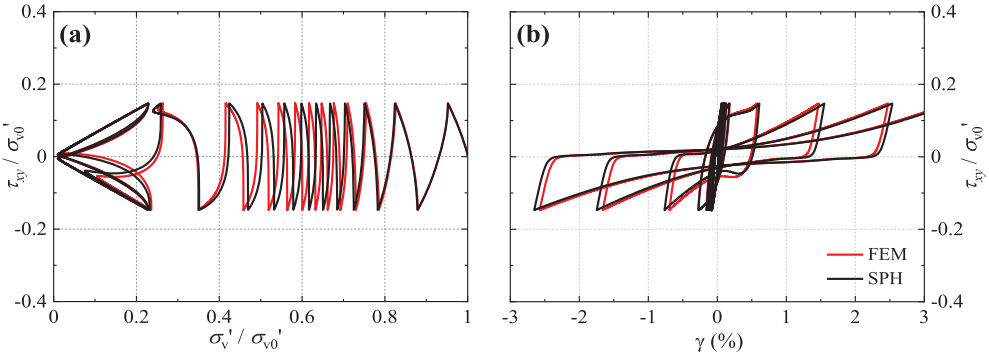

Figure 5: Cyclic direct simple shear at $(N_1)_{60} = 14$ (a) effective stress path and (b) stress-strain response

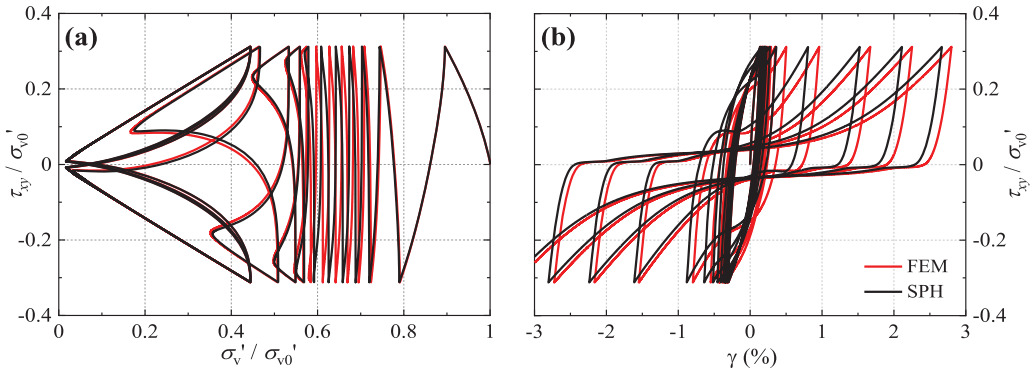

Figure 6: Cyclic direct simple shear at $(N_1)_{60} = 26$ (a) effective stress path and (b) stress-strain response

6.2 Seismic Analysis of Level Ground Site

Following the verification of the PM4Sand model implementation in the previous section, the SPH framework is now adopted to analyze a more generalized scenario representative of actual field conditions. Specifically, the seismic response analysis of a level ground site comprising a layered soil deposit is carried out using the proposed SPH framework and compared with benchmark results from OpenSees [68]. The site conditions, SPH, and FEM models are shown in Fig. 7. The site consists of three soil layers with SPT $(N_1)_{60}$ values of 6, 14, and 26 for Layers 1, 2, and 3, respectively, while the groundwater table is at the surface (Fig. 7a). The present example demonstrates the capability of the SPH framework to capture the seismic response of a site consisting of soils with different initial densities. Further, the analysis also serves as a validation case for the compliant base and free field boundary conditions proposed in Section 4.

Two SPH models, SPH A (Fig. 7b) and SPH B (Fig. 7c), are utilised for the analysis. In SPH A, a 1 m wide soil column, along with periodic boundary conditions, is used for modeling an infinitely wide, horizontal soil domain. SPH B consists of a 5 m wide main domain region, along with lateral boundary regions of 1 m width on either side. The boundary regions act as fixed support and free field columns during the static and seismic analysis, respectively (Section 4). Thus, SPH A and B differ only in terms of the lateral boundary conditions. The periodic boundaries in SPH A approximate an infinitely wide, horizontal soil domain without the requirement of any lateral boundaries, allowing the validation of the compliant base boundary condition. Subsequently, SPH B is utilized for validating the free field boundary condition by comparing the response to SPH A and FEM results. It is noteworthy that, as the main domain region in SPH B does not contain any secondary structure (e.g., earth dam), the response of SPH A and B to seismic loading is expected to be similar.

The primary calibration parameters for the PM4Sand model used in the SPH and FEM analyses are summarised in Table 1. Further, the specific gravity of soil solids $G_s = 2.67$, unit weight of water $\gamma_f = 10$ kNm^{-3}, and the isotropic hydraulic conductivity $k = 1.0 \times 10^{-3}$ ms^{-1}. Spatial discretisation in SPH is carried out using particles (velocity nodes) placed at an initial spacing of 0.2 m and two stress nodes per velocity node (Fig. 1). On the other hand, 40 nine-node quadrilateral elements (9_4_QuadUP) of dimension 1 m $\times$ 0.5 m are used for the FEM analysis (Fig. 7d).

The initial effective stress state is generated using the gravity loading method in both SPH and FEM analysis. During the gravity loading phase, the Poisson's ratio ν is assigned such that $K_0 = 0.5$. A fully fixed (no-slip) condition is assigned to the base boundary for both SPH models, whereas the lateral boundaries in SPH B are modeled as free-slip. Further, hydraulic boundary conditions of zero

pressure head at the free surface and impermeability at the base are imposed. For the FEM analysis, the base is modeled as fully fixed, while nodes at the same elevation are assigned an equal degree of freedom condition [51]. After the gravity loading analysis, Poisson's ratio is reset to the default value of 0.3, as recommended for the PM4Sand model [44].

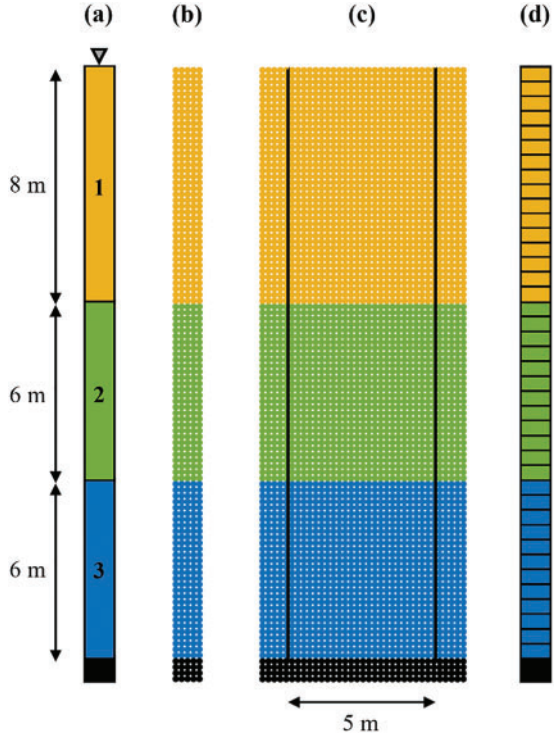

Figure 7: Seismic analysis of level ground site (a) site conditions, (b) SPH model A, (c) SPH model B, and (d) FEM model

The soil columns are subjected to the earthquake signal shown in Fig. 8. The acceleration history (Fig. 8a) is the horizontal component of the signal RSN765 recorded at Gilroy Array #1 during the 1989 Loma Prieta earthquake and has a peak acceleration of 0.47 g. The velocity history (Fig. 8b) is obtained by integrating the acceleration signal and represents the outcrop motion. Thus, the input to the SPH model (Eq. (14)) is half of the $v - t$ signal shown in Fig. 8b. For the seismic analysis, the base boundary condition in SPH and FEM are modified to free-slip and roller support, respectively. The fixed lateral boundaries in SPH B are replaced by free field columns whose motion is solved independently using periodic boundary conditions. The ground motion is applied to the SPH and FEM models using the compliant base conditions. The viscous dashpots for the compliant base (Eq. (14)) are assigned the properties of soil layer 3 to prevent stress wave reflection. Local damping coefficient $\xi_l = 0.05$ during the seismic analysis.

The horizontal component of the free-surface acceleration and the corresponding response spectrum at a 5% damping ratio for the SPH and FEM analysis is shown in Fig. 9a,b, respectively. The free-surface acceleration in SPH is calculated using the interpolation equation Eq. (10). The peak acceleration from the three numerical models are 0.145 g (SPH A), 0.148 g (SPH B), and 0.150 g (FEM). Thus, the SPH analyses capture the peak and frequency content of the surface acceleration with satisfactory accuracy. The discrepancies in the SPH and FEM results may be attributed to the

difference in the numerical discretization of the coupled flow-deformation model and the nature of the temporal integration scheme (i.e., explicit leapfrog method in SPH and implicit Newmark method in FEM). Nevertheless, the SPH framework satisfactorily captures the essential information necessary for engineering analysis and design.

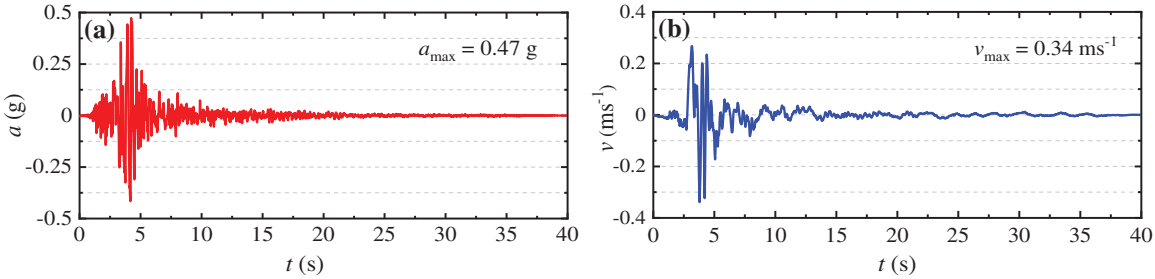

Figure 8: Input signal for seismic analysis of level ground site (a) acceleration, (b) velocity-time histories

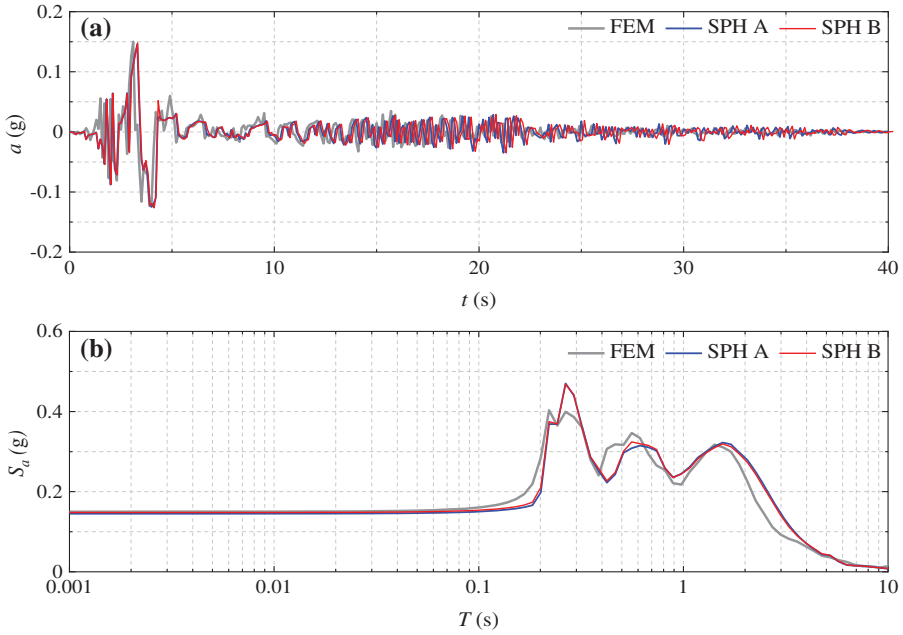

Figure 9: (a) Horizontal acceleration-time history at the free surface and (b) response spectrum at 5% damping ratio

The development of excess pore-water pressure ratio r_u ($= \Delta p_f / \sigma'_{v0}$) in SPH A is shown in Fig. 10. Similar results are also obtained for SPH B and are not shown here. The loose sand layer (Layer 1) develops high excess pore-water pressure and reaches liquefaction ($r_u \approx 1$) during the strong ground motion period. Excess pore-water pressure is developed in the denser Layers 2 and 3; however, it is insufficient to cause liquefaction for the applied earthquake signal. The excess pore-water pressure dissipates after the strong ground motion period until $r_u \approx 0$, i.e., the hydrostatic conditions are attained. The r_u from the SPH analyses are compared to FEM results at the mid-depth of the three layers, i.e., at 4, 11, and 17 m from the surface (Fig. 11). As shown in Fig. 11, the development and dissipation of the excess pore-water pressure in the soil layers are captured with satisfactory accuracy.

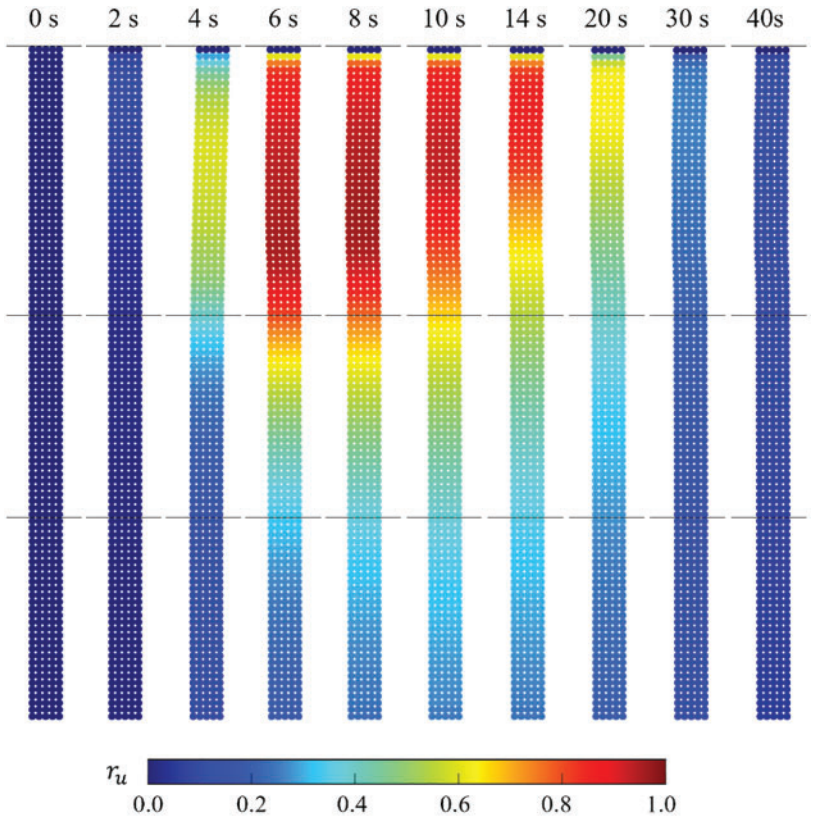

Figure 10: Excess pore-water pressure ratio (r_u) in SPH A during the earthquake

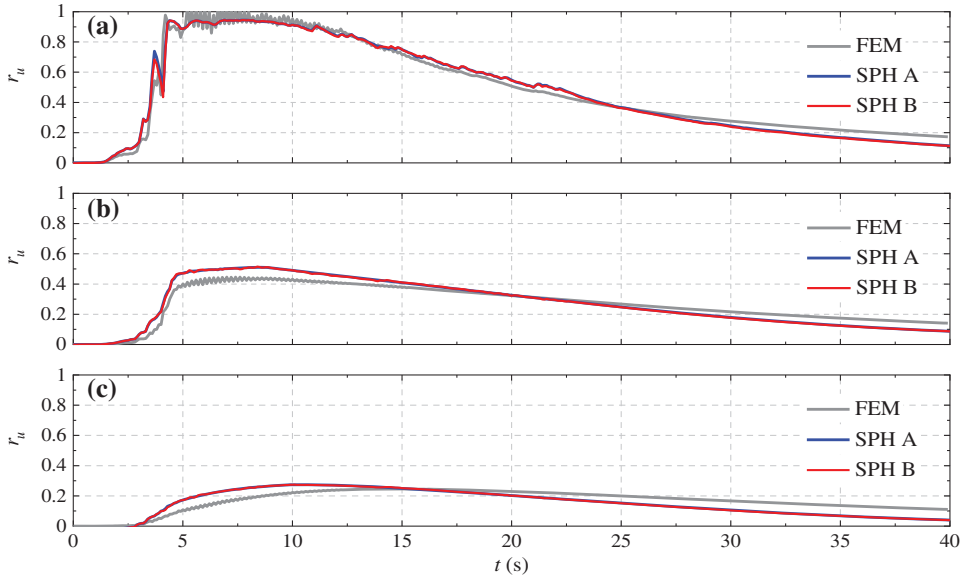

Figure 11: Excess pore-water pressure ratio (r_u) at (a) 4 m, (b) 11 m, and (c) 17 m from the surface

The modification to the periodic boundary conditions proposed in Section 4 allows the lateral sway of the soil column to be observed during seismic loading (Fig. 10). The soil column demonstrates level ground liquefaction where ground oscillation is produced during the earthquake; however, the residual lateral deformation at the end of ground motion is small [1]. The response of FEM, SPH A and B in terms of the surface acceleration and development of excess pore-water pressure are almost identical, thus validating the compliant base and free field boundary conditions proposed in Section 4. The results of the seismic analysis of the level ground site demonstrate that the SPH framework is capable of modeling soil liquefaction for practical geotechnical engineering scenarios.

6.3 Liquefaction-Induced Failure of the Lower San Fernando Dam

A seismic response analysis of the Lower San Fernando Dam (LSFD) is carried out in this section to demonstrate the capability of the SPH framework to capture liquefaction-induced large deformation failures of complex geotechnical structures. The idealised cross-section of LSFD developed by Seed et al. [70] is illustrated in Fig. 12. The dam's height is 44 m with upstream and downstream slopes of 1 V:2.5 H and 1 V:4 H, respectively. The earth dam was primarily constructed using the hydraulic fill method, resulting in a cohesive central clay core (CC) and a cohesionless shell (regions HFU 1 to 4 on the upstream and HFD 1 to 4 on the downstream side). Ground shale (GS) and rolled fill (RF) layers were placed to raise the dam's height to the required level. A chimney drain and rolled fill (RF) berm were also constructed along the downstream slope to improve stability. The foundation consisted of upper alluvium (UA) and lower alluvium (LA) layers under stiff bedrock. The reservoir level was 338 m, whereas the downstream water level is assumed to be at the surface (305 m). Additional details on the construction methodology can be found in [12].

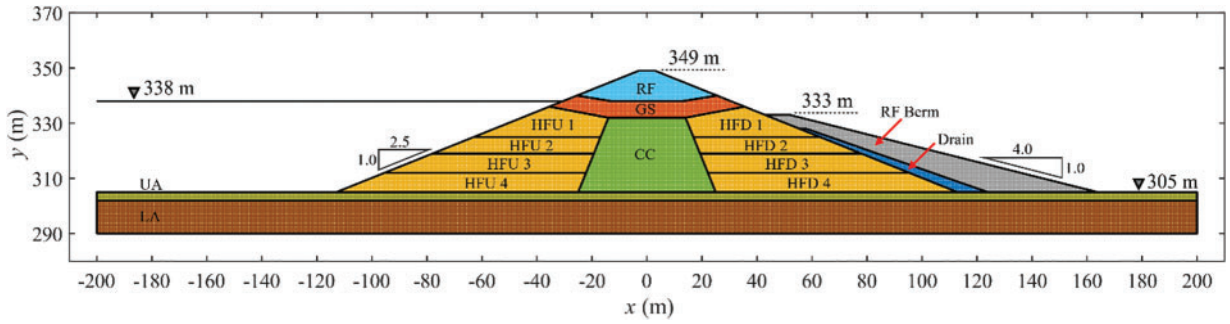

Figure 12: Geometry and initial conditions for the analysis of the Lower San Fernando Dam

The upstream slope of the LSFD suffered a large deformation flow failure during the 1971 San Fernando Earthquake [12]. The upstream toe was displaced by 42 to 65 m into the reservoir, resulting in the settlement of the crest and almost a complete loss of the reservoir freeboard. Only minor deformations were observed on the downstream slope. Post-failure site investigation [70] identified the cause of the flow failure to be the liquefaction of the hydraulically filled shell (i.e., HFU 1 to 4 and HFD 1 to 4). Notably, liquefaction was not observed for the other soils. The geotechnical properties of the materials in LSFD are summarised in Table 2 [12].

Table 2: Geotechnical properties of the materials in Lower San Fernando Dam

Soil	c' (kPa)	ϕ' (^{0})	$\gamma_{bulk}/\gamma_{sat}$ (kNm^{-3})	k_v (ms^{-1})	k_h/k_v	G (kPa)	K (kPa)
LA	0	37	19.5/20.4	1.0×10^{-7}	4	1.0×10^{5}	3.0×10^{5}
UA	0	37	19.5/20.4	1.0×10^{-7}	4	9.6×10^{4}	2.9×10^{5}
CC	0	30	18.1/18.9	5.0×10^{-8}	4	6.3×10^{4}	1.9×10^{5}
GS	23.9	27	18.9/19.8	1.0×10^{-7}	4	9.9×10^{4}	3.0×10^{5}
RF	14.4	31	20.4/21.2	5.0×10^{-6}	1	9.1×10^{4}	2.7×10^{5}
Drain	0	37	18.9/19.6	1.0×10^{-5}	1	8.7×10^{4}	2.6×10^{5}
RF Berm	4.8	37	19.5/20.4	5.0×10^{-6}	1	9.1×10^{4}	2.7×10^{5}
HFU 1	0	35	18.9/19.8	5.0×10^{-7}	10	8.0×10^{4}	2.4×10^{5}
HFU 2	0	34	18.9/19.8	5.0×10^{-7}	10	7.5×10^{4}	2.3×10^{5}
HFU 3	0	36	19.0/20.1	1.0×10^{-7}	10	8.7×10^{4}	2.6×10^{5}
HFU 4	0	33	18.9/19.8	5.0×10^{-7}	10	7.4×10^{4}	2.2×10^{5}
HFD 1	0	35	18.9/19.8	1.0×10^{-7}	10	8.0×10^{4}	2.4×10^{5}
HFD 2	0	34	18.9/19.8	1.0×10^{-7}	10	7.5×10^{4}	2.3×10^{5}
HFD 3	0	36	19.0/20.1	2.0×10^{-8}	10	8.7×10^{4}	2.6×10^{5}
HFD 4	0	33	18.9/19.8	1.0×10^{-7}	10	7.4×10^{4}	2.2×10^{5}

Note: c' = effective cohesion intercept; ϕ' = effective angle of shearing resistance; γ_{bulk} = bulk unit weight; γ_{sat} = saturated unit weight; k_v = vertical hydraulic conductivity; k_h = horizontal hydraulic conductivity; G = secant shear modulus; K = bulk modulus; ϕ' of clay core estimated using liquid limit based correlation [71].

Spatial discretisation of the numerical model is performed using approximately 20,000 particles (velocity nodes) at an initial spacing $\Delta x = 0.8$ m and two stress nodes per velocity node (Fig. 1). The particle spacing is selected after verifying the convergence of the numerical results with respect to the particle spacing. Steady-state seepage analysis is carried out by solving the flow model (Eq. (7)) with soil deformation neglected and a reduced bulk modulus of water ($K_l = 1.0 \times 10^3$ kPa) [72]. The hydraulic boundary conditions for the flow model are (i) impermeable condition along the base (Eq. (12)), (ii) constant total head on upstream and downstream free surfaces below the respective water levels, and (iii) seepage surface boundary condition on the surfaces exposed to the atmosphere and along the chimney drain and rock fill berm [48]. After the steady state seepage condition is achieved, the gravity loading analysis is carried out using the Drucker Prager model for all soils with the material properties summarised in Table 2. The boundary conditions for the static analysis include full fixity (no-slip) at the base and free-slip on the lateral boundaries. The pre-earthquake pore-water pressure and effective vertical stress are shown in Fig. 13.

For the seismic analysis, the material model of the liquefiable soil layers (i.e., HFU 1 to 4 and HFD 1 to 4) is changed to PM4Sand. In contrast, the non-liquefiable soils are described using the Drucker Prager model. The PM4Sand model is initialised using the pre-earthquake effective stress following the procedure outlined in [51]. Chowdhury [12] utilised the finite difference package FLAC [73] for the seismic analysis of LSFD using the PM4Sand model. The PM4Sand model was calibrated to best match the post-failure field observations. In the present study, the PM4Sand calibration parameters reported by Chowdhury [12] (Table 3) are adopted for the seismic analysis to enable a straightforward comparison with the results reported in that study. Additionally, Chowdhury [12], based on a comprehensive review of the literature related to LSFD, stated that no reliable ground motion measurements were available for the LSFD site. As a result, Chowdhury [12] recommended that

the acceleration-time history recorded at the nearby Pacoima dam (RSN77 in the PEER database), rotated to a direction transverse to the crest of LSFD and scaled to a peak acceleration of 0.80 g be adopted for the seismic analysis. The scaling factor was deduced based on an assessment of the expected ground motions at the LSFD site, considering the effect of local geology using the modern NGA-West2 ground motion prediction equations [67]. Further, the scaling factor was corroborated by a series of simulations of possible slip mechanism scenarios during the 1971 San Fernando earthquake. As a result, the scaled ground motion represents the best estimate of the ground motion at LSFD. A detailed discussion of various aspects related to the input ground motion for seismic analysis of LSFD can be found in [12]. In the present study, the numerical model is subjected to the ground motion shown in Fig. 14, adopted from Doan et al. [19]. The velocity history (Fig. 14b) is obtained by integrating the acceleration signal. Half of the velocity signal (Fig. 14b) is applied as input to the SPH model using Eq. (14). The base boundary condition is modified to free slip to transfer the ground motion to the numerical model accurately. Further, the fixed lateral boundaries are replaced by free field columns following the procedure outlined in Section 4. The ground motion is applied using the compliant base boundary conditions with the viscous dashpots assigned the properties of the lower alluvium, local damping coefficient $\xi_l = 0.05$ during the seismic analysis.

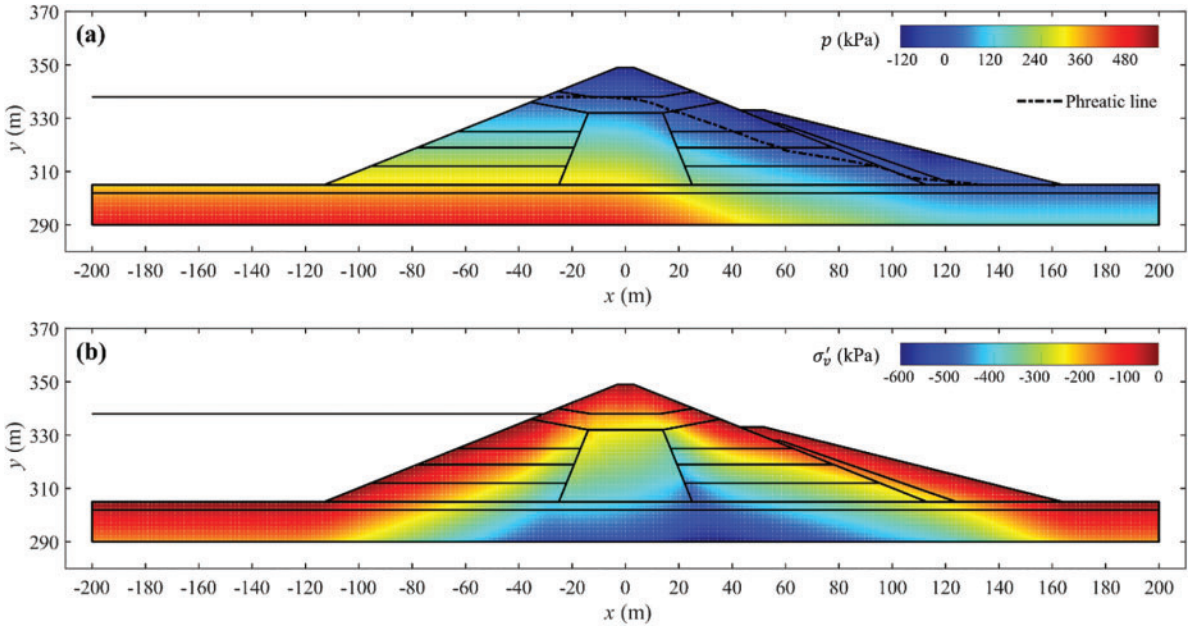

Figure 13: Pre-earthquake conditions in LSFD (a) pore-water pressure and (b) effective vertical stress

Table 3: PM4Sand calibration parameters for hydraulic filled shell in LSFD

Soil layer	$(N_1)_{60}$	D_r	G_0	h_{p0}
HFU 1/HFD 1	16.6	0.62	729.8	0.15
HFU 2/HFD 2	14.2	0.57	682.5	0.12
HFU 3/HFD 3	19.5	0.67	783.3	0.23
HFU 4/HFD 4	12.8	0.54	653.2	0.11

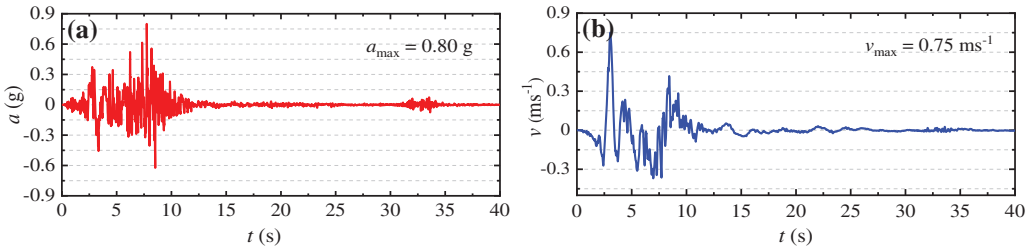

Figure 14: Input signal for seismic analysis of LSFD (a) acceleration and (b) velocity-time histories

Fig. 15a,b illustrates the maximum excess pore-water pressure ratio and shear strain in the hydraulic filled shell developed during the earthquake. The excess pore-water pressure ratio is calculated as $r_u = 1 - \sigma_v'/\sigma_{v0}'$ where σ_v' and σ_{v0}' are the current and pre-earthquake vertical effective stresses. As shown in Fig. 15a,b, high excess pore-water pressure and shear strains are developed in the hydraulic filled shell, particularly in the relatively loose HFU 2 and 4 layers on the upstream and HFD 2 and 4 layers on the downstream side. As a result, the hydraulically filled shell can be expected to contribute to post-earthquake instability. Additionally, a crest settlement of approximately 2.2 m is observed at the end of the ground motion (Fig. 15c). The results of the seismic analysis, i.e., maximum excess pore-water pressure ratio, shear strain, and crest settlement during the earthquake, are in satisfactory agreement with the FLAC analysis of Chowdhury [12].

The large deformation flow behaviour is governed by the shear strength of the liquefied soil. However, the PM4Sand model does not implicitly transition to the post-liquefaction residual shear strength during the application of the ground motion to the numerical model [12]. As a result, the commonly adopted approach is to identify the elements or particles that undergo liquefaction and assign post-liquefaction residual shear strength for the post-earthquake analysis. A soil element or node is considered to be liquefied if the maximum excess pore-water pressure ratio $r_{u,max} \geq 0.7$ during shaking or the shear strain $\gamma \geq 10\%$ at the end of shaking [12,19]. The post-earthquake undrained analysis of the liquefied soils is then carried out in a total stress framework using elastoplastic soil models developed for static analysis (e.g., Drucker Prager or Mohr-Coulomb) [74]. However, the above-described approach was found to result in numerical instabilities in the SPH analysis, particularly along the free surface of the submerged upstream slope and at the interface between the liquefied and the non-liquefied soil regions. Notably, the liquefaction-triggering aspects of the LSFD have already been well captured, as shown in Fig. 15. To validate the capabilities of the SPH framework in modeling the post-liquefaction large deformation behaviour, a simplified post-earthquake analysis is carried out to capture the general characteristics of the flow slide at LSFD.

The liquefied soil is described by an effective stress analysis using the Drucker Prager model. The ϕ' of the liquefied soil is calibrated to best match the field observed elevation of the upstream slide heel scarp (point **A** in Fig. 16). The final elevation of the heel scarp was a critical factor that prevented catastrophic overtopping of the dam, and as a result, is selected for calibration. Fig. 16 shows the final deformation profile of LSFD using calibrated parameters, i.e., $\phi' = 5$ degrees for the liquefied and 30 degrees for the non-liquefied soil regions of the hydraulic filled shell. The following field-observed features of the failure could be captured by the simplified post-earthquake analysis (i) the numerically simulated elevation of the heel scarp is approximately 339.0 m compared to the field observed 339.5 m [12], (ii) the major flow slide of the upstream slope with a toe runout distance of approximately 55 m, and (iii) minor deformations on the downstream slope due to the stabilising effect of the rolled fill berm. However, the numerically simulated failure mechanism differs from the field observation of intact blocks of non-liquefied soil sliding over the liquefied soil [12,31,70].

Talbot et al. [31] demonstrated that the failure mechanism of LSFD can be accurately captured if total stress (undrained) analysis is carried out for all soils in the post-earthquake phase, given the relatively rapid deformations at LSFD. Nevertheless, such an analysis is not further pursued in this study, as the numerical results adequately demonstrate the capability of the SPH framework for modeling the triggering of liquefaction and post-liquefaction large deformations of a complex geotechnical structure.

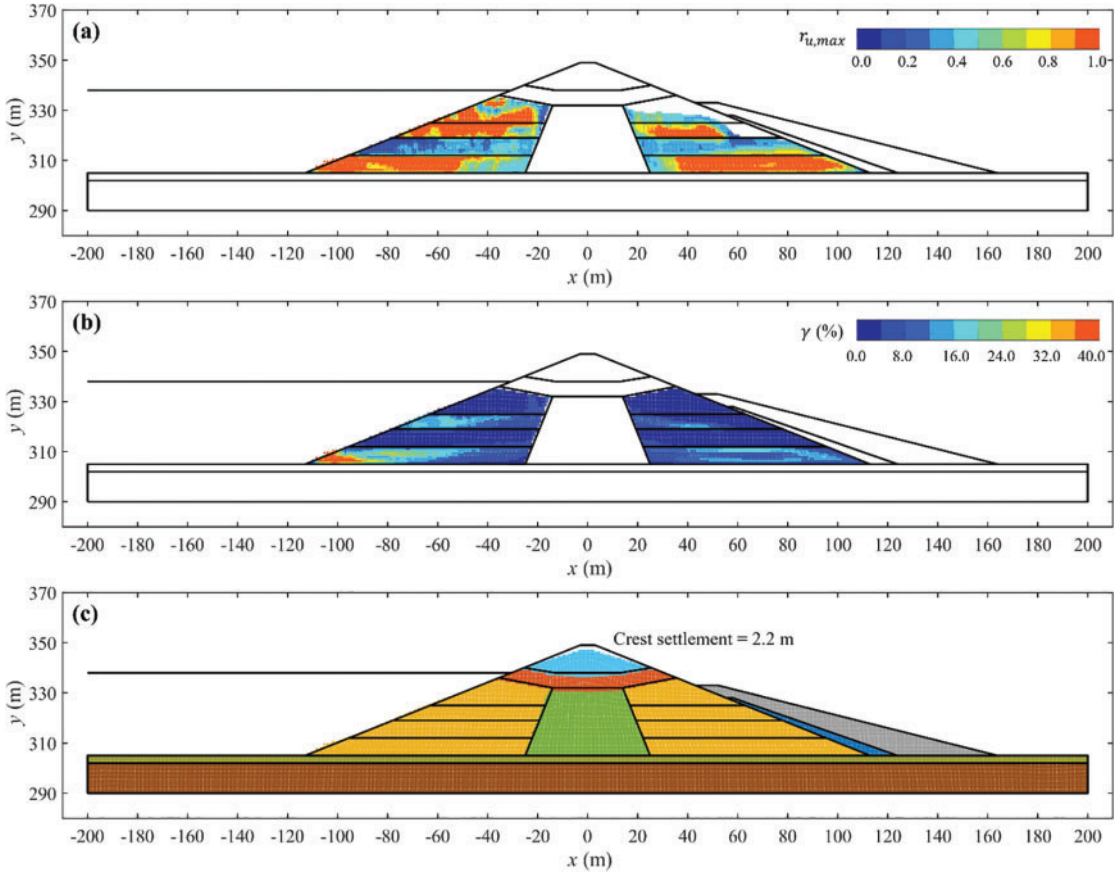

Figure 15: (a) Maximum excess pore-water pressure ratio in the hydraulic filled shell, (b) shear strain in the hydraulic filled shell, and (c) crest settlement at the end of the earthquake

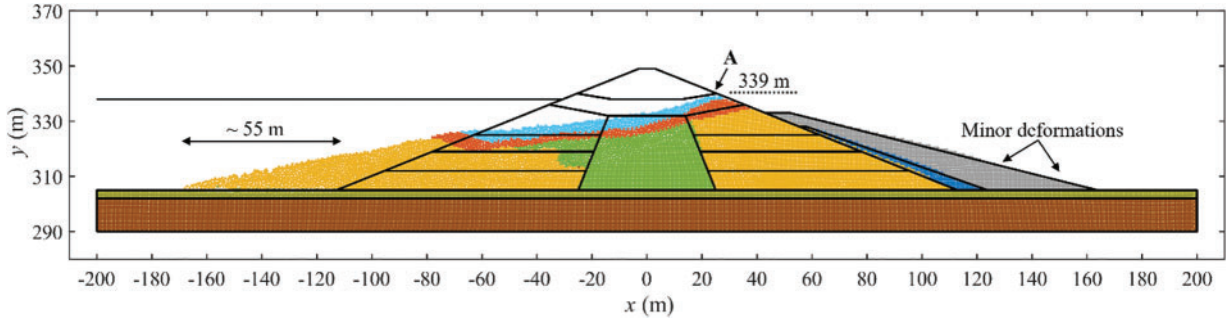

Figure 16: Final deformation profile for the Lower San Fernando Dam

7 Discussion

Section 6 demonstrates that the proposed SPH framework can model soil liquefaction with satisfactory accuracy. The results of the SPH analysis are consistent with FEM simulations or results from published studies for liquefaction triggering. Additionally, owing to the meshless nature of the method, the post-liquefaction large deformation behaviour can also be analysed, making the framework suitable for liquefaction hazard assessment.

Numerical analysis of seismic hazards (such as liquefaction) remains a continually evolving field, driven by advancements in computational techniques and a deepening understanding of soil behaviour under cyclic loading conditions. The present study is expected to serve as the foundation for further development of SPH-based numerical techniques that contribute to safer and more resilient geotechnical structures in seismically active areas. In this regard, a few essential features of the proposed SPH framework and associated limitations that can be addressed by future studies are further elaborated in this section.

7.1 Constitutive Model

- The PM4Sand model has been developed to emulate field observations and empirical correlations for soil liquefaction commonly employed in earthquake geotechnical engineering [51]. The model has been extensively utilized in liquefaction studies due to its satisfactory performance in reproducing laboratory and field observations and the relative ease of calibration based on a few parameters that can be derived from routine geotechnical investigations. Accordingly, the present study adopts the PM4Sand model to describe the behaviour of the liquefiable soils subjected to cyclic loading.
- The PM4Sand model can be calibrated to capture a wide range of behaviours related to pore-water pressure generation and cyclic strains. Nevertheless, the present study adopts the PM4Sand calibration parameters from the literature to validate the various aspects of the proposed SPH framework by comparing the numerical results with benchmark FEM simulations or field observations reported in the published studies.
- It is noteworthy that using predefined PM4Sand calibration parameters for validation does not affect the generalizability of the various components of the proposed SPH framework (e.g., spatial discretization and boundary conditions). Accordingly, the SPH framework can be used for predictive analysis by calibrating the PM4Sand model using laboratory and field observations following the procedure described in [43,44].
- Although the PM4Sand model has been extensively adopted for liquefaction analysis, no single constitutive model can fully capture the complex behaviour of soils under all conditions. As a result, a comparison between the numerical accuracy of various constitutive models implemented within the SPH framework is essential. Although the substitution of constitutive models is straightforward due to the modular nature of the SPH framework, such an exercise is not carried out in the present study.
- Further, the PM4Sand model is only applicable for two-dimensional (plane-strain) analysis, and alternate soil models will be necessary to extend the SPH framework for three-dimensional scenarios.

7.2 Boundary Conditions & Input Ground Motion

- Non-reflecting (absorbing) boundary conditions for seismic analysis using the SPH method are proposed in Section 4. The numerical examples demonstrate that the boundary conditions can

accurately transfer the ground motion and model the non-reflecting conditions. Although the focus of the present study is soil liquefaction, the boundary conditions are generalized and can also be applied for modeling (i) other seismic hazards, such as seismically induced landslides, (ii) blast-induced soil liquefaction, or (iii) dynamic soil-structure interaction problems in semi-infinite or infinite soil domains.

- The earthquake ground motion is imposed as a traction time history based on the principles of stress wave propagation in elastic media (Eqs. (14) and (15)). Thus, the artificial boundaries should be sufficiently far away from the region of major deformations to ensure low strain levels at the boundary.
- The ground motion signal is applied uniformly over the compliant base boundary in the form of vertically propagating stress waves. In reality, such a condition can only be assumed after the seismic waves have traveled a considerable distance from the earthquake source and have been subjected to multiple refractions [1]. As a result, applying a non-uniform ground motion signal will be essential for the analysis of sites that are relatively near the earthquake source.
- For modeling the lateral non-reflecting boundaries, the fixed boundary particles used in the static analysis are replaced by free field columns. The motion of the free field particles is solved independently using periodic boundary conditions to approximate infinitely wide, horizontal soil domains. Additionally, the free field particles interact with the main domain region (Fig. 2). As a result, the complexity of the numerical algorithm is enhanced due to the requirement of additional particle interactions. Moreover, the computational efficiency is reduced as neighbour search and particle interactions are often the most computationally expensive operations in particle-based methods.
- The modification to the periodic boundary conditions allows the lateral sway of the free field columns to be modeled. Nevertheless, some particle disorder in the main domain region near the lateral boundaries may still be observed due to the application of the viscous dashpot forces as point loads. However, the effect of particle disorder on the numerical results is expected to be minimal as the lateral boundaries are required to be sufficiently away from the regions of significant deformations to satisfy the assumption of elastic wave propagation.
- The seismic analyses in Sections 6.2 and 6.3 were carried out using representative ground motions (Figs. 8 and 14) for validating the various aspects of the SPH framework by comparing the results with FEM simulations or published studies. In general, ground motion characteristics, i.e., peak ground acceleration (PGA), frequency content, and duration of ground motion, directly influence the nonlinear seismic response of soil deposits as well as the built infrastructure on it. Specifically, (i) a higher PGA indicates a higher intensity of ground shaking and higher inertial loads, (ii) frequency content governs potential resonance scenarios, where high amplitude vibrations occur if the ground motion frequency matches the natural frequency of the structure, and (iii) a higher duration of ground motion leads to a higher excess pore-water pressure accumulation and stiffness degradation. The ground motion characteristics are dictated by the geological conditions of a site (i.e., the soil or rock type). Hence, when employing the SPH framework for predictive analysis, selecting ground motion representative of the site-specific conditions is fundamental for achieving accurate and reliable seismic response.
- Earthquake-induced ground motion is typically recorded at rock outcrops. However, for seismic analysis, the input ground motion must be specified at the level of the compliant base boundary. Accordingly, an equivalent linear deconvolution analysis of the rock outcrop motion will be necessary to obtain the appropriate input ground motion for the SPH model [1].

7.3 Validation of the SPH Framework Using Field Data

- A potential limitation of the present study is that the validation is performed using only FEM simulations or results from published studies. It is acknowledged that further validation based on field data is fundamental to establishing the SPH framework for seismic analysis of geotechnical structures. Such an exercise is being undertaken by integrating field data collected using static and seismic Cone Penetration Tests (CPTs) and Hydraulic Profiling Tool (HPT) at an earth dam site in India into the proposed SPH framework.
- Nevertheless, the comprehensive statistical validation of the framework prediction with the field measured data, as well as the sensitivity analysis to assess the numerical stability and robustness of the framework, is beyond the scope of the present study and will be reported in our future works.

7.4 Computational Expense of the SPH Framework

- The present study adopts the single-layer SPH discretization wherein the fluid phase is described in an Eulerian reference frame moving with the soil phase. Although the single-layer approach is efficient for large-scale applications [45,56], the computational expense is still significantly higher than mesh-based methods (i.e., FEM or FDM). As a result, mesh-based methods may be preferred over SPH for seismic analysis when material deformations are limited or when the post-failure large deformation behaviour is not of concern.
- For large deformation analysis, a hybrid numerical approach using mesh-based and meshless SPH methods for the pre-and post-failure analysis, respectively, can be adopted to improve the overall computational efficiency. However, the hybrid approach is not suitable for coseismic deformation scenarios wherein large deformations may be observed during the ground motion period, which is often resolved using mesh-based techniques [33].
- On the other hand, the SPH approach can effectively cater to both small and large deformation scenarios, as demonstrated by the present study. Specifically, for the seismic analysis of a level ground site (Section 6.2), the soil profile demonstrates lateral deformation during the ground motion period. However, the final displacement is small (Fig. 10). In contrast, the liquefaction-induced failure of the Lower San Fernando Dam (Section 6.3) illustrates the capability of the framework in capturing liquefaction triggering and gravity-driven mass flow involving large deformations (Fig. 16).
- Nevertheless, the computational efficiency of the algorithm and the SPH framework needs to be improved to allow large-scale or three-dimensional analysis. For this purpose, parallelization techniques based on CPUs or GPUs are available [75–79]. However, such a development is beyond the scope of the present study.

8 Conclusions

This study presents a numerical framework for the earthquake-induced liquefaction hazard assessment of geotechnical structures based on a three-phase, single-layer SPH approach, with the behaviour of soils subjected to cyclic loading described using the PM4Sand model. The spatial discretisation is carried out using the stress particle SPH method to minimise the effects of zero-energy modes and tensile instability on the numerical solution. Additionally, compliant base and free field boundary conditions appropriate for the SPH method are proposed, allowing the numerical treatment of unbounded (semi-infinite) soil domains. Numerical analysis of (i) cyclic direct simple shear test, (ii) seismic response of a level ground site, and (iii) liquefaction-induced failure of the Lower San Fernando

Dam is carried out to demonstrate that the SPH framework can model the liquefaction triggering, as well as the post-liquefaction large deformation behaviour with satisfactory accuracy. Although the present study is primarily targeted toward soil liquefaction, the proposed SPH framework is versatile and can be adapted for modeling other scenarios of soil subjected to cyclic loading (e.g., seismically induced landslides). Such applications will be explored in future studies to enhance the understanding and management of seismic hazards.

Acknowledgement: This research did not receive any specific grant from funding agencies in the public, commercial, or not-for-profit sectors. This study is inspired by an extensive association (from investigation stage onwards) in the analysis and design of the Main Dam of Polavaram Irrigation Project, India through several agencies such as the Water Resources Department, Andhra Pradesh, India; Megha Engineering and Infrastructure Limited; Navayuga Engineering Company. The insights gained through these works, particularly from projects IITD/IRD/CW14168, CW14469, and CW14378, have significantly contributed to the development of the analysis presented in this study.

Funding Statement: The authors received no specific funding for this study.

Author Contributions: The authors confirm their contribution to the paper as follows: study conception and design: Sourabh Mhaski, G. V. Ramana; analysis and interpretation of results: Sourabh Mhaski, G. V. Ramana; draft manuscript preparation: Sourabh Mhaski; review & editing: G. V. Ramana. All authors reviewed the results and approved the final version of the manuscript.

Availability of Data and Materials: Data sharing is not applicable to this article as no datasets were generated or analysed during the current study.

Ethics Approval: Not applicable.

Conflicts of Interest: The authors declare no conflicts of interest to report regarding the present study.

References

1. Kramer SL. Geotechnical earthquake engineering. Upper Saddle River, New Jersey, USA: Prentice-Hall; 1996.
2. Xu C, Ma S, Tan Z, Xie C, Toda S, Huang X. Landslides triggered by the 2016 Mj 7.3 Kumamoto, Japan, earthquake. Landslides. 2018;15(3):551–64. doi:10.1007/s10346-017-0929-1.
3. Bhattacharya S, Hyodo M, Nikitas G, Ismael B, Suzuki H, Lombardi D, et al. Geotechnical and infrastructural damage due to the 2016 Kumamoto earthquake sequence. Soil Dyn Earthq Eng. 2018;104(1):390–4. doi:10.1016/j.soildyn.2017.11.009.
4. Bhattacharya S, Hyodo M, Goda K, Tazoh T, Taylor CA. Liquefaction of soil in the Tokyo Bay area from the 2011 Tohoku (Japan) earthquake. Soil Dyn Earthq Eng. 2011;31(11):1618–28. doi:10.1016/j.soildyn.2011.06.006.
5. Bray JD, Markham CS, Cubrinovski M. Liquefaction assessments at shallow foundation building sites in the central business district of christchurch, New Zealand. Soil Dyn Earthq Eng. 2017;92(4):153–64. doi:10.1016/j.soildyn.2016.09.049.
6. Sonmez B, Ulusay R, Sonmez H. A study on the identification of liquefaction-induced failures on ground surface based on the data from the 1999 Kocaeli and Chi-Chi earthquakes. Eng Geol. 2008;97(3–4):112–25. doi:10.1016/j.enggeo.2007.12.008.

7. Yoshida N, Watanabe H, Yasuda S, Mora Castro S. Liquefaction-induced ground failure and related damage to structures during 1991 Telire-Limon, Costa Rica, earthquake. In: Proceedings from the Fourth Japan-US Workshop on Earthquake Resistant Design of Lifeline Facilities and Countermeasures for Soil Liquefaction, 1992; HI, USA: p. 37–52.
8. Seed RB, Dickenson SE, Idriss IM. Principal geotechnical aspects of the 1989 Loma Prieta earthquake. Soils Found. 1991;31(1):1–26. doi:10.3208/sandf1972.31.1.
9. Soga K. Soil liquefaction effects observed in the Kobe earthquake of 1995. Proc Inst Civ Eng Geotech Eng., 1998;131(1):34–51. doi:10.1061/JSFEAQ.0001260.
10. Seed HB, Idriss IM. Influence of soil conditions on ground motions during earthquakes. J Soil Mech Found Div. 1969;95(1):99–137. doi:10.1061/JSFEAQ.0001260.
11. Elia G, Rouainia M. Advanced dynamic nonlinear schemes for geotechnical earthquake engineering applications: a review of critical aspects. Geotech Geol Eng. 2022;40(7):3379–92. doi:10.1007/s10706-022-02109-6.
12. Chowdhury KH. Evaluation of the state of practice regarding nonlinear seismic deformation analyses of embankment dams subject to soil liquefaction based on case histories (Ph.D. Thesis). University of California: Berkeley; 2018.
13. Chan AHC, Pastor M, Schrefler BA, Shiomi T, Zienkiewicz OC. Computational geomechanics: theory and applications. Hoboken, NJ, USA: John Wiley & Sons; 2022.
14. Cui CY. Seismic behavior and reinforcement mechanisms of earth dam and liquefiable foundation system by shaking table tests and numerical simulation. Soil Dyn Earthq Eng. 2023;173(5):108083. doi:10.1016/j.soildyn.2023.108083.
15. Li G, Motamed R. Finite element modeling of soil-pile response subjected to liquefaction-induced lateral spreading in a large-scale shake table experiment. Soil Dyn Earthq Eng. 2017;92(3):573–84. doi:10.1016/j.soildyn.2016.11.001.
16. Kang GC, Tobita T, Iai S. Seismic simulation of liquefaction-induced uplift behavior of a hollow cylinder structure buried in shallow ground. Soil Dyn Earthq Eng. 2014;64(1):85–94. doi:10.1016/j.soildyn.2014.05.006.
17. Tang XW, Zhang XW, Uzuoka R. Novel adaptive time stepping method and its application to soil seismic liquefaction analysis. Soil Dyn Earthq Eng. 2015;71(9):100–13. doi:10.1016/j.soildyn.2015.01.016.
18. Qiu Z, Lu J, Elgamal A, Su L, Wang N, Almutairi A. OpenSees three-dimensional computational modeling of ground structure systems and liquefaction scenarios. Comput Model Eng Sci. 2019;120(3):629–56. doi:10.32604/cmes.2019.05759.
19. Doan NP, Nguyen BP, Park SS. Seismic deformation analysis of earth dams subject to liquefaction using UBCSAND2 model. Soil Dyn Earthq Eng. 2023;172:108003. doi:10.1016/j.soildyn.2023.108003.
20. Boulanger RW, Montgomery J. Nonlinear deformation analyses of an embankment dam on a spatially variable liquefiable deposit. Soil Dyn Earthq Eng. 2016;91(3):222–33. doi:10.1016/j.soildyn.2016.07.027.
21. Liu Y, Chen X, Hu M. Three-dimensional large deformation modeling of landslides in spatially variable and strain-softening soils subjected to seismic loads. Can Geotech J. 2023;60(4):426–37.
22. Liu S, Tang X, Li J. A decoupled Arbitrary Lagrangian-Eulerian method for large deformation analysis of saturated sand. Soils Found. 2022;62(2):101110. doi:10.1016/j.sandf.2022.101110.
23. Zhuang H, Hu Z, Wang X, Chen G. Seismic responses of a large underground structure in liquefied soils by FEM numerical modelling. Bull Earthq Eng. 2015;13(12):3645–68.
24. Liang W, Zhao J, Wu H, Soga K. Multiscale, multiphysics modeling of saturated granular materials in large deformation. Comput Methods Appl Mech Eng. 2023;405:115871. doi:10.1016/j.cma.2022.115871.
25. Qin J, Mei G, Xu N. Meshfree methods in geohazards prevention: a survey. Arch Comput Methods Eng. 2022;29(5):3151–82. doi:10.1007/s11831-021-09686-4.

26. Bui HH, Nguyen GD. Smoothed particle hydrodynamics (SPH) and its applications in geomechanics: from solid fracture to granular behaviour and multiphase flows in porous media. Comput Geotech. 2021;138(5):104315. doi:10.1016/j.compgeo.2021.104315.
27. Soga K, Alonso E, Yerro A, Kumar K, Bandara S, Kwan JSH, et al. Trends in large-deformation analysis of landslide mass movements with particular emphasis on the material point method. Geotechnique. 2018;68(5):457–8. doi:10.1680/jgeot.15.LM.005.
28. Sizkow SF, El Shamy U. SPH-DEM modeling of the seismic response of shallow foundations resting on liquefiable sand. Soil Dyn Earthq Eng. 2022;156(3):107210. doi:10.1016/j.soildyn.2022.107210.
29. Sizkow SF, El Shamy U. SPH-DEM simulations of saturated granular soils liquefaction incorporating particles of irregular shape. Comput Geotech. 2021;134(3):104060. doi:10.1016/j.compgeo.2021.104060.
30. El Shamy U, Sizkow SF. Coupled SPH-DEM simulations of liquefaction-induced flow failure. Soil Dyn Earthq Eng. 2021;144(3):106683. doi:10.1016/j.soildyn.2021.106683.
31. Talbot LED, Given J, Tjung EYS, Liang Y, Chowdhury K, Seed R, et al. Modeling large-deformation features of the Lower San Fernando Dam failure with the material point method. Comput Geotech. 2024;165(2):105881. doi:10.1016/j.compgeo.2023.105881.
32. Zai D, Pang R, Xu B, Liu J. Seismic failure probability analysis of slopes via stochastic material point method. Soil Dyn Earthq Eng. 2023;172(2):108041. doi:10.1016/j.soildyn.2023.108041.
33. Kohler M, Stoecklin A, Puzrin AM. A MPM framework for large-deformation seismic response analysis. Can Geotech J. 2022;59(6):1046–60. doi:10.1139/cgj-2021-0252.
34. Kohler M, Puzrin AM. Mechanism of Co-Seismic deformation of the slow-moving la sorbella landslide in italy revealed by MPM analysis. J Geophys Res Earth Surf. 2022;127(7):1–25. doi:10.1029/2022JF006618.
35. Giridharan S, Gowda S, Stolle DFE, Moormann C. Comparison of UBCSAND and hypoplastic soil model predictions using the material point method. Soils Found. 2020;60(4):989–1000. doi:10.1016/j.sandf.2020.06.001.
36. Mao Z, Liu G, Huang Y, Bao Y. A conservative and consistent Lagrangian gradient smoothing method for earthquake-induced landslide simulation. Eng Geol. 2019;260(9):105226. doi:10.1016/j.enggeo.2019.105226.
37. Chen W, Qiu T. Simulation of earthquake-induced slope deformation using SPH method. Int J Numer Anal Methods Geomech. 2014;38(3):297–330.
38. Bui HH, Fukagawa R, Sako K, Okamura Y. Earthquake induced slope failure simulation by SPH. In: International Conference on Recent Advances in Geotechnical Earthquake Engineering and Soil Dynamics, 2010; San Diego, CA, USA.
39. Shuai H, Liu CZ, Katsuichiro G. Applicability of smooth particle hydrodynamics method to large sliding deformation of saturated slopes under earthquake action. Chinese J Geotech Eng. 2023;45(2):336–44 (In Chinese).
40. Bao Y, Huang Y, Liu GR, Wang G. SPH simulation of high-volume rapid landslides triggered by earthquakes based on a unified constitutive Model. Part I: initiation process and slope failure. Int J Comput Methods. 2020;17(4):1850150. doi:10.1142/S0219876218501505.
41. Zhang W, Yu R, Chen Y, Chen S. SPH analysis of sliding material volume and influence range of soil slope under earthquake. Front Phys. 2022;10:1–9.
42. Huang Y, Li G, Xiong M. Stochastic assessment of slope failure run-out triggered by earthquake ground motion. Nat Hazards. 2020;101(1):87–102. doi:10.1007/s11069-020-03863-7.
43. Boulanger RW, Ziotopoulou K. Formulation of a sand plasticity plane-strain model for earthquake engineering applications. Soil Dyn Earthq Eng. 2013;53(6):254–67. doi:10.1016/j.soildyn.2013.07.006.
44. Ziotopoulou K, Boulanger RW. Plasticity modeling of liquefaction effects under sloping ground and irregular cyclic loading conditions. Soil Dyn Earthq Eng. 2016;84(1):269–83. doi:10.1016/j.soildyn.2016.02.013.

45. Lian Y, Bui HH, Nguyen GD, Zhao S, Haque A. A computationally efficient SPH framework for unsaturated soils and its application to predicting the entire rainfall-induced slope failure process. Geotechnique. 2022;74(8):787–805.
46. Chalk CM, Pastor M, Peakall J, Borman DJ, Sleigh PA, Murphy W, et al. Stress-particle smoothed particle hydrodynamics: an application to the failure and post-failure behaviour of slopes. Comput Methods Appl Mech Eng. 2020;366(1):113034. doi:10.1016/j.cma.2020.113034.
47. Randles PW, Libersky LD. Normalized SPH with stress points. Int J Numer Methods Eng. 2000;48(10):1445–62. doi:10.1002/1097-0207(20000810)48:10<1445::AID-NME831>3.0.CO;2-9.
48. Lian Y, Bui HH, Nguyen GD, Tran HT, Haque A. A general SPH framework for transient seepage flows through unsaturated porous media considering anisotropic diffusion. Comput Methods Appl Mech Eng. 2021;387:114169. doi:10.1016/j.cma.2021.114169.
49. Dafalias YF, Manzari MT. Simple plasticity sand model accounting for fabric change effects. J Eng Mech. 2004;130(6):622–34. doi:10.1061/(ASCE)0733-9399(2004)130:6(622).
50. Manzari MT, Dafalias YF. A critical state two-surface plasticity model for sands. Géotechnique. 1997;47(2):255–72. doi:10.1680/geot.1997.47.2.255.
51. Chen L, Arduino P. Implementation, verification, and validation of the PM4Sand model in OpenSees. Berkeley: University of California, Pacific Earthquake Engineering Research Center; PEER Report No. 2021/02. doi: 10.55461/SJEU6160.
52. Dinesh N, Banerjee S, Rajagopal K. Performance evaluation of PM4Sand model for simulation of the liquefaction remedial measures for embankment. Soil Dyn Earthq Eng. 2022;152(5):107042. doi:10.1016/j.soildyn.2021.107042.
53. Bui HH, Fukagawa R, Sako K, Ohno S. Lagrangian meshfree particles method (SPH) for large deformation and failure flows of geomaterial using elastic-plastic soil constitutive model. Int J Numer Anal Methods Geomech. 2008 Aug 25;32(12):1537–70. doi:10.1002/nag.688.
54. Monaghan JJ. Smoothed particle hydrodynamics and its diverse applications. Annu Rev Fluid Mech. 2011;44:323–46.
55. Violeau D, Rogers BD. Smoothed particle hydrodynamics (SPH) for free-surface flows: past, present and future. J Hydraul Res. 2016;54(1):1–26. doi:10.1080/00221686.2015.1119209.
56. Mhaski S, Ramana GV. Modelling coupled flow-solute transport in porous media using smoothed particle hydrodynamics (SPH). Comput Geotech. 2024;167:106097. doi:10.1016/j.compgeo.2024.106097.
57. Bui HH, Fukagawa R. An improved SPH method for saturated soils and its application to investigate the mechanisms of embankment failure: case of hydrostatic pore-water pressure. Int J Numer Anal Methods Geomech. 2013 Jan 1;37(1):31–50. doi:10.1002/nag.1084.
58. Feng R, Fourtakas G, Rogers BD, Lombardi D. A general smoothed particle hydrodynamics (SPH) formulation for coupled liquid flow and solid deformation in porous media. Comput Methods Appl Mech Eng. 2024;419(5):116581. doi:10.1016/j.cma.2023.116581.
59. Liu MB, Liu GR. Restoring particle consistency in smoothed particle hydrodynamics. Appl Numer Math. 2006;56(1):19–36. doi:10.1016/j.apnum.2005.02.012.
60. Marrone S, Antuono M, Colagrossi A, Colicchio G, Le Touzé D, Graziani G. δ-SPH model for simulating violent impact flows. Comput Methods Appl Mech Eng. 2011;200(13–16):1526–42. doi:10.1016/j.cma.2010.12.016.
61. English A, Domínguez JM, Vacondio R, Crespo AJC, Stansby PK, Lind SJ, et al. Modified dynamic boundary conditions (mDBC) for general-purpose smoothed particle hydrodynamics (SPH): application to tank sloshing, dam break and fish pass problems. Comput Part Mech. 2022;9(5):1–15. doi:10.1007/s40571-021-00403-3.
62. Lysmer J, Kuhlemeyer RL. Finite dynamic model for infinite media. J Eng Mech Div. 1969;95(4):859–77. doi:10.1061/JMCEA3.0001144.

63. Allen MP, Tildesley DJ. Computer simulation of liquids. Oxford, UK: Oxford University Press; 2017.
64. Mhaski S, Ramana GV. Risk assessment of municipal solid waste (MSW) dumps using two-phase Random SPH: case study of three dumpsites. Comput Part Mech. 2023;11(1):359–388. doi:10.1007/s40571-023-00627-5.
65. Mhaski S, Ramana GV. Internal erosion induced instability of coal ash ponds: forensic analysis using smoothed particle hydrodynamics (SPH). Comput Geotech. 2024;173:106558. doi:10.1016/j.compgeo.2024.106558.
66. Verrucci L, Pagliaroli A, Lanzo G, Di Buccio F, Biasco AP, Cucci C. Damping formulations for finite difference linear dynamic analyses: performance and practical recommendations. Comput Geotech. 2022;142(5):104568. doi:10.1016/j.compgeo.2021.104568.
67. Ancheta TD, Darragh RB, Stewart JP, Seyhan E, Silva WJ, Chiou BSJ, et al. NGA-West2 database. Earthq Spectra. 2014;30(3):989–1005.
68. McKenna F, Scott MH, Fenves GL. Nonlinear finite-element analysis software architecture using object composition. J Comput Civ Eng. 2010;24(1):95–107.
69. Boulanger RW, Ziotopoulou K. PM4Sand (Version 3.1): a sand plasticity model for earthquake engineering applications. California: University of California Davis, Center for Geotechnical Modeling, Department of Civil and Environmental Engineering; 2017. Report No. UCD/CGM-15/01.
70. Seed HB, Idriss IM, Lee KL, Makdisi FI. Dynamic analysis of the slide in the Lower San Fernando Dam during the earthquake of February 9, 1971. J Geotech Eng Div. 1975;101(9):889–911.
71. Lambe TW, Whitman RV. Soil mechanics, New York, USA: John Wiley & Sons; 1969.
72. Ma G, Bui HH, Lian Y, Tran KM, Nguyen GD. A five-phase approach, SPH framework and applications for predictions of seepage-induced internal erosion and failure in unsaturated/saturated porous media. Comput Methods Appl Mech Eng. 2022;401:115614. doi:10.1016/j.cma.2022.115614.
73. Itasca. Fast lagrangian analysis of continua, version 7.0. Minneapolis, Minnesota: Itasca Consulting Group, Inc.; 2011.
74. Boulanger RW, Kamai R, Ziotopoulou K. Liquefaction induced strength loss and deformation: simulation and design. Bull Earthq Eng. 2014;12(3):1107–28.
75. Ricci F, Vacondio R, Tafuni A. Multiscale smoothed particle hydrodynamics based on a domain-decomposition strategy. Comput Methods Appl Mech Eng. 2024;418(3):116500. doi:10.1016/j.cma.2023.116500.
76. Chen D, Yao X, Huang D, Huang W. A multi-resolution smoothed particle hydrodynamics with multi-GPUs acceleration for three-dimensional fluid-structure interaction problems. Ocean Eng. 2024;296(21):117017. doi:10.1016/j.oceaneng.2024.117017.
77. Liu J, Yang X, Zhang Z, Liu M. A massive MPI parallel framework of smoothed particle hydrodynamics with optimized memory management for extreme mechanics problems. Comput Phys Commun. 2024;295(2):108970. doi:10.1016/j.cpc.2023.108970.
78. Guo X, Rogers BD, Lind S, Stansby PK. New massively parallel scheme for Incompressible Smoothed Particle Hydrodynamics (ISPH) for highly nonlinear and distorted flow. Comput Phys Commun. 2018;233(2):16–28. doi:10.1016/j.cpc.2018.06.006.
79. Crespo AJC, Domínguez JM, Rogers BD, Gómez-Gesteira M, Longshaw S, Canelas R, et al. DualSPHysics: open-source parallel CFD solver based on Smoothed Particle Hydrodynamics (SPH). Comput Phys Commun. 2015;187(6):204–16. doi:10.1016/j.cpc.2014.10.004.